CrossMark

Surveying the Giant H II Regions of the Milky Way with SOFIA. VI. NGC 3603

James M. De Buizer[1,4] , Wanggi Lim[2] , Nicole Karnath[3] , and James T. Radomski[1]

[1] SOFIA-USRA, NASA Ames Research Center, Mail Stop 232-12, Moffett Field, CA 94035, USA; jdebuizer.astro@gmail.com
[2] IPAC, Mail Code 100-22, Caltech, 1200 E. California Blvd., Pasadena, CA 91125, USA
[3] Space Science Institute, 4765 Walnut Street, Suite B, Boulder, CO 80301, USA

Abstract

We present our sixth set of results from our mid-infrared imaging survey of Milky Way Giant H II regions with our detailed analysis of NGC 3603, the most luminous giant H II (GH II) region in the Galaxy. We used imaging data from the FORCAST instrument on the Stratospheric Observatory For Infrared Astronomy (SOFIA) at 20 and 37 μm, which mapped the central $\sim 8\rlap{.}'5 \times 8\rlap{.}'5$ infrared-emitting area of NGC 3603 at a spatial resolution of $\lesssim 3''$. Utilizing these SOFIA data in conjunction with multiwavelength observations from the near-infrared to radio, including Spitzer-IRAC and Herschel-PACS archival data, we investigate the physical nature of individual infrared sources and subcomponents within NGC 3603. For individual compact sources, we used the multiwavelength photometry data to construct spectral energy distributions (SEDs) and fit them with massive young stellar object (MYSO) SED models, and find 14 sources that are likely to be MYSOs. We also detect dust emission from the 3 massive proplyd candidates, as well as from the disk and outflow of the evolved blue supergiant, Sher 25. Utilizing multiwavelength data, we derived luminosity-to-mass ratio and virial parameters for the star-forming clumps within NGC 3603, estimating their relative ages and finding that NGC 3603 is an older GH II region overall, compared to our previously studied GH II regions. We discuss how NGC 3603, which we categorize as a *cavity-type* GH II region, exhibits a more modest number of MYSOs and molecular clumps when compared to the *distributed-type* GH II regions that share similar Lyman continuum photon rates.

1. Introduction

Massive stars form in giant molecular clouds where they initially tend to be highly embedded and hence visible only in mid-infrared to submillimeter wavelengths. Eventually, the central protostar reaches such high temperatures that it begins to produce substantial amounts of Lyman continuum photons. These photons create an ionized region in the star's immediate surroundings, which is bright in centimeter radio continuum emission. In the case of a large cluster of massive stars, or multiple generations of massive star formation, the combined Lyman continuum emission can ionize vast regions within the clusters' host molecular cloud, resulting in the creation of a giant H II (GH II) region. These objects typically have sizes of 3–20 pc in the infrared, and have Lyman continuum photon rates in excess of 10^{50} photons s^{-1}.

Compared to low-mass star formation, less is known about the environments of and processes that govern massive star ($M > 8\,M_\odot$) formation. However, understanding massive star formation is crucial since massive stars are responsible for the creation and distribution of most heavy elements in a galaxy, and are therefore ultimately responsible for the chemical building blocks necessary for the creation of other stars, planets, and life as we know it. Since GH II regions are the most intense sites of star formation that exist in regular galaxies

like the Milky Way, they offer a unique opportunity to study massive star-forming clusters and their environments.

In a series of papers starting with Lim & De Buizer (2019; hereafter Paper I), we have been studying the infrared properties of Galactic GH II regions using newly acquired data from the Stratospheric Observatory for Infrared Astronomy (SOFIA), as well as archival data from the Spitzer and Herschel infrared space telescopes. Our source list of 42 bona fide GH II regions and GH II region candidates comes from De Buizer et al. (2022; hereafter Paper IV), which was adapted from the original census of Conti & Crowther (2004) who identified GH II region candidates from published 6 cm all-sky surveys along with infrared data from the Midcourse Space Experiment (MSX) and Infrared Astronomical Satellite (IRAS) archives. The original aim of our survey was to produce 20 and 37 μm maps of as many of the GH II regions from the census as we could with SOFIA, and use that data (along with other multiwavelength data) to understand their physical properties individually and as a population. However, with the recent cancellation of the SOFIA program, our project will remain incomplete with only 29% of the total population observed (i.e., 12/42 GH II regions). Nonetheless, we will continue to concentrate on studying the infrared properties of each remaining GH II region for which we have data, comparing and contrasting each region to those regions previously studied in this series. In this, the sixth paper of the series, we will focus on the well-known GH II region, NGC 3603.

In terms of Lyman continuum photon rate $(4.1 \times 10^{51}$ photons s^{-1}; Paper IV), NGC 3603 is the most powerful GH II region in the Galaxy. At its heart lies a young, massive OB cluster named HD 97950, which is believed to be one of

---

[4] Corresponding author.

the few Galactic starburst clusters in the Milky Way, containing more than 70 O stars (Moffat et al. 1994) as well as 3 Wolf–Rayet stars (Melnick et al. 1989; Hofmann et al. 1995) and possessing a dynamic stellar cluster mass of almost 18,000 $M_\odot$ (Rochau et al. 2010). This powerful cluster has been carving out a bubble in the molecular cloud hosting NGC 3603, leading to a rather small A_V ($\sim$4.5 mag; Eisenhauer et al. 1998) along the line of sight to the cluster, as well as creating pillars/elephant trunks in the surrounding molecular cloud. It is believed that this expansion into the surrounding molecular cloud may also be triggering the present star formation occurring in NGC 3603 (e.g., Röllig et al. 2011). Compared to our closest massive star-forming cluster, the Trapesium in Orion, the NGC 3603 star cluster has about 100 times more ionizing power. Given its relatively close proximity (7.2 ± 0.1 kpc[5]; Drew et al. 2019), NGC 3603 is invaluable in that it can be studied in rather fine detail and can be used as a proxy in understanding extragalactic starburst phenomena.

In Section 2, we discuss the new SOFIA observations and give information on the data obtained. In Section 3, we give more background on NGC 3603 as we compare our new data to previous observations and discuss individual sources and regions in-depth. In Section 4, we discuss our data analysis, modeling, and derivation of physical parameters of sources and regions. We also discuss our interpretation of these results. Our conclusions are summarized in Section 5.

2. Observations and Data Reduction

The observational techniques and reduction processes employed on the data were, for the most part, identical to those described in Paper I for W51A. Below, we will highlight some of the observation and reduction details specific to these new observations of NGC 3603. For a more in-depth discussion of these details and techniques, refer to Paper I.

Observations were made with the airborne astronomical observatory, SOFIA (Young et al. 2012), utilizing the FORCAST instrument (Herter et al. 2013). Data were taken of NGC 3603 across four nights, 2019 July 2–5, (Flight Numbers 589–592) with the SOFIA aircraft temporarily deployed to and flying sorties out of Christchurch, New Zealand. All observations were taken at altitudes between 41,000 and 43,000 ft, which typically yields precipitable water vapor overburdens of 4–7 μm at the latitudes where the observations occurred ($-35°$ to $-65°$). FORCAST is a facility imager and spectrograph that employs a Si:As 256×256 blocked-impurity band (BIB) detector array to cover a wavelength range of 5–25 μm and a Si:Sb 256×256 BIB array to cover the range from 25 to 40 μm. Observations were obtained in the 20 μm ($\lambda_{eff} = 19.7$ μm; $\Delta\lambda = 5.5$ μm) and 37 μm ($\lambda_{eff} = 37.1$ μm; $\Delta\lambda = 3.3$ μm) filters simultaneously using an internal dichroic. In imaging mode, the arrays cover a $3'.40 \times 3'.20$ instantaneous field of view with a pixel scale of $0''.768$ pixel^{-1} after distortion correction.

All images were obtained by employing the standard chop-nod observing technique used in ground-based thermal infrared observing, with chop throws of up to $7'$ and nod throws of up to $16'$ in order to be sufficiently large enough to sample clear off-source sky regions uncontaminated by the extended emission of NGC 3603. The mid-infrared emitting area of NGC 3603 is much larger than the FORCAST field of view, and thus had to

be mapped using multiple pointings. Each of the eight individual pointings had an average on-source exposure time of about 300 s at both 20 and 37 μm. The SOFIA Data Pipeline software produced the final mosaicked images (Level 4 data products) from the eight individual pointing images, and these final mosaicked images are presented and used here in this work.

Flux calibration for each source was provided by the SOFIA Data Cycle System pipeline, and the final total photometric errors in the images were derived using the same process described in Paper I. The estimated total photometric errors are 15% for 20 μm and 10% for 37 μm.

The image quality for SOFIA is typically $\sim$2″.5 (FWHM) resolution at 20 μm and $\sim$3″.1 at 37 μm. However, on Flights 588–592, there were issues with the chopping secondary mirror, which lead to elongated point-spread functions in the chop direction, and the amount of elongation varied from negligible to twice the normal FWHM. The chop direction was changed from pointing to pointing, and thus so did the direction of elongation. Therefore, in the final mosaicked image, the point sources may appear elongated and in different directions depending on their location within NGC 3603.

The final mosaics also had their astrometry absolutely calibrated using Spitzer data by matching up the centroids of point sources in common between the Spitzer and SOFIA data. The absolute astrometry of the final SOFIA images is assumed to be better than 2″.0, which is a more conservative estimate than that quoted in our previous papers (i.e., 1″.0–1″.5) due to the poorer image quality and because of changes in the focal plane distortion and our ability to accurately correct it with the limited calibration data available for these observations.

In addition to the SOFIA data, we also utilize science-ready imaging data from the Spitzer Space Telescope and Herschel Space Telescope archives. Figure 1 shows a four-color composite image made from the SOFIA 20 and 37 μm data (blue and green, respectively), the Herschel 70 μm imaging data (red), and the Spitzer-IRAC 3.6 μm imaging data (white). Figure 2 shows just the 20 μm SOFIA final imaging mosaic, and Figure 3 shows just the 37 μm SOFIA final imaging mosaic.

3. Comparing SOFIA Images of NGC 3603 to Previous Imaging Observations

Since most GH II regions are buried deep within giant molecular clouds, NGC 3603 is somewhat rare in that it is rather optically bright, which is why observations of this object date back to its discovery by Sir John Herschel in 1834. There is consequently a wealth of optical and near-infrared data on NGC 3603 (e.g., Goss & Radhakrishnan 1969; Brandl et al. 1999; Nürnberger et al. 2002), especially concerning the stellar cluster HD 97590 (which can be seen just below the center of Figure 1) and its immediate environment (e.g., Melnick et al. 1989; Eisenhauer et al. 1998; Brandner et al. 2000), including high-resolution (0″.2) Hubble Space Telescope (HST) images (Moffat et al. 1994). The copious Lyman continuum photons and strong stellar winds from this central stellar cluster can be seen in these optical and near-infrared images to have carved out a large gas-free cavity in the surrounding molecular material. This results in large gaseous pillars on the cavity walls, as well as shaping three compact objects that look like externally irradiated protostellar objects (Brandner et al. 2000;

---

[5] For more on this adopted distance, see Appendix B.

Figure 1. A four-color image of the central ∼8′.5 × 8′.5 (19.6 × 19.6 pc) region of NGC 3603. Blue is the SOFIA-FORCAST 20 μm image, green is the SOFIA-FORCAST 37 μm image, and red is the Herschel-PACS 70 μm image. Overlaid in white is the Spitzer-IRAC 3.6 μm image, which traces the revealed stars within NGC 3603, field stars, and hot dust.

Mücke et al. 2002) known as "proplyds," which were first seen in Orion (Bally et al. 2000).

The first radio continuum images of NGC 3603 were presented in Goss & Radhakrishnan (1969), where they showed a single, extended 6 cm continuum source at ∼3′ resolution peaked on and coincident with the extended Hα (656 nm) nebular emission. Later, the 21 cm maps of Retallack & Goss (1980) at 50″ resolution resolved the region into two main emission areas, G291.59-0.50, which lies to the north of the revealed massive stellar cluster HD 97950, and G291.63-0.54, which lies to the south. It then took almost until the turn of the twenty-first century for higher angular resolution radio images to appear, with the ∼7″ images at 3.4 cm of those from De Pree et al. (1999) taken with the Australia Telescope Compact Array. With a factor of ∼7 times better angular resolution, De Pree et al. (1999) identified 13 peaks in the extended radio emission, which were labeled A through M (see labels on Figures 2 and 3, which show the positions of the radio peaks). Later observations by Mücke et al. (2002) imaged the central 3′ area at ∼1″ resolution at 3 and 6 cm.

Similar to the radio continuum observations, there has been a lack of high angular resolution mid-infrared imaging of NGC 3603. Frogel et al. (1977) were the first to show 10 and 20 μm maps of NGC 3603, which had about 15″ angular

resolution, as well as 2.2 μm maps with 22″ resolution. They were able to detect the two prominent peaks in the area at 10 and 20 μm, the first associated with the E radio peak (which they labeled IRS 1), and the second associated with the F–I radio area (which they labeled IRS 2). A third peak was also seen at 10 and 20 μm (named IRS 3), but it is not associated with any radio source. They found several additional 2.2 μm point sources (labeled IRS 4–IRS 15), and using additional J and H data, they were able to determine that IRS 9, which is the only 2.2 μm source found within their 10 and 20 μm emission region, was highly reddened. These mid-infrared observations were followed by those of Lacy et al. (1982) who mapped only the IRS 1 and IRS 2 regions in the spectral lines of Ne II and S IV at 7″ resolution.

The next observations in the mid-infrared of NGC 3603 were not until those of Nürnberger & Stanke (2003), who attempted to map the region at ∼1″ resolution using the ESO 3.6 m telescope at 12 and 18 μm. However, this facility can only chop and nod up to 20″, and the infrared-emitting area of NGC 3603 is much larger. This means their background reference beams were full of emission, and therefore, the accuracy of their maps and the photometry of sources were compromised by false structures due to poor background subtraction. Furthermore, unlike the larger coverage of their 12 μm map, their shallow
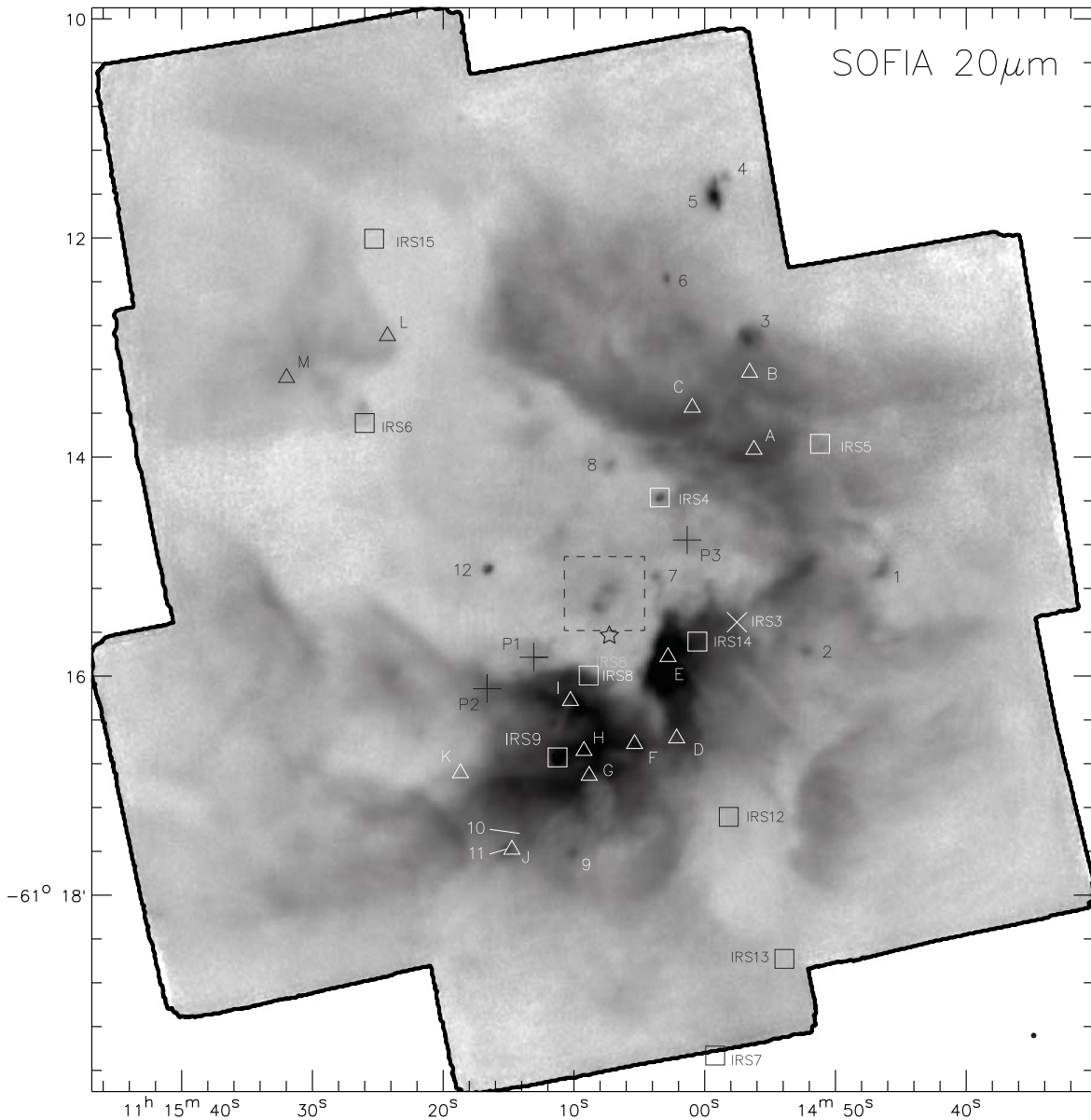
Figure 2. NGC 3603 image mosaic taken at 20 μm by SOFIA shown in inverse color (i.e., brighter features are darker in color). Sources discussed in the text are labeled: the star show the location of the approximate center of the HD 97590 OB star cluster, the triangles are the locations of radio continuum peaks from De Pree et al. (1999), squares are the locations of previously identified near-infrared sources (see Table 1), crosses mark the location of the proplyds, and numbers label the mid-infrared compact sources identified in this work. The dashed square surrounds the source Sher 25 and has the approximate field size displayed in Figure 11. The black dot in the lower right indicates the resolution of the image at this wavelength.

18 μm map only covered the IRS 1 and IRS 2 area. Shortly thereafter in the mid-2000s, Spitzer-IRAC imaging of NGC 3603 generated fine images of the entirety of NGC 3603 in the near-infrared (3.6, 4.5, and 5.8 μm); though, the mid-infrared 8 μm images are plagued with cosmetic issues due to saturation on the brightest point sources on the field. Additionally, the Spitzer-MIPS imaging data at 24 μm and longer wavelengths are saturated almost entirely throughout the central $8' \times 8'$ area (Gvaramadze et al. 2013). Similarly, images were taken at 3.4, 4.6, 12, and 22 μm of NGC 3603 with the Wide-field Infrared Survey Explorer (WISE) satellite; however, the two mid-infrared wavelengths (12 and 22 μm) were also entirely saturated. The only images obtained of the entire mid-infrared emitting area of NGC 3603 in the last four decades that were unsaturated and unaffected by spurious background subtraction were those from the MSX satellite, which had a

resolution of ∼18″ at 21 μm (see Wang & Chen 2010), and the SOFIA 20 and 37 μm images at ∼3″ resolution presented here.

In terms of large-scale structure, the SOFIA 20 and 37 μm images look fairly similar to each other. However, looking at the four-color image in Figure 1, it can be seen that there is a distinct blue haze around and interior to the green and red areas of NGC 3603. Since blue is the 20 μm SOFIA image and the shortest wavelength of the three, the areas dominated by emission in this filter are likely to be tracing the hotter dust closer to the central stellar cluster. The green and red regions (corresponding to the brighter areas in the SOFIA 37 μm and Herschel 70 μm data, respectively) trace the colder dust, and thus, the emission is offset farther from the heating of the central cluster. At these wavelengths, emission can also be seen coming from the various pillars and trunks, all of which point back to HD 97590.
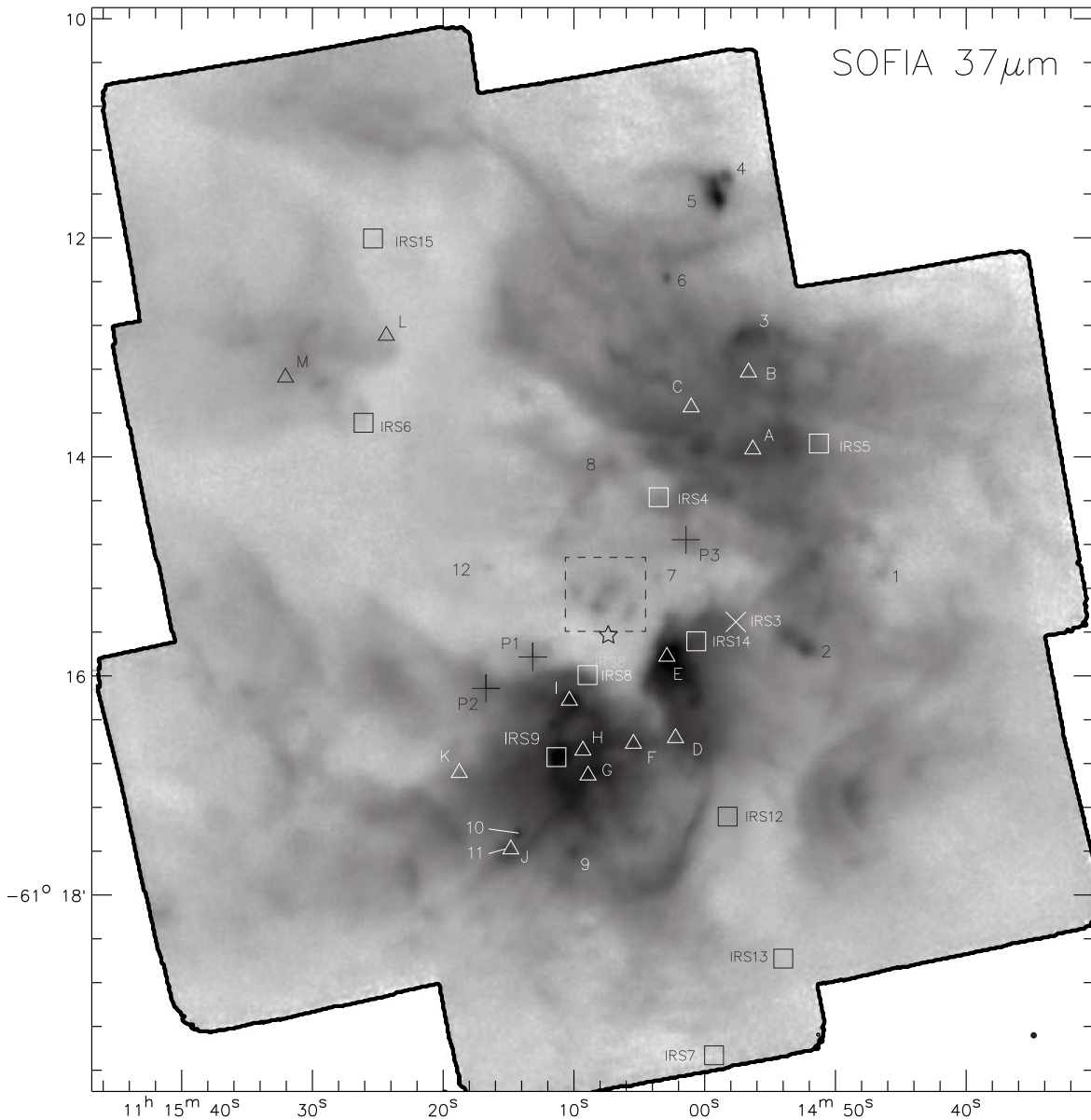
Figure 3. NGC 3603 image mosaic taken at 37 μm by SOFIA. See caption of Figure 2 for explanation of symbols and figure annotation.

3.1. Discussion of Individual Sources in NGC 3603

Here, we will discuss the individual infrared sources detected by SOFIA within NGC 3603 and compare them to previous multiwavelength observations. We will also discuss the nature of the individual sources, where possible. This will often include our findings from the spectral energy distribution (SED) modeling that we will describe in detail in Section 4.1, which is based upon the infrared photometry of the SOFIA, as well as Spitzer and Herschel data. Please refer to that section for more detailed information regarding how the SED analyses were performed.

3.1.1. Source 1

Source 1 appears as a point source in the Spitzer-IRAC 3.6 and 4.5 μm images (Figure 4) with an arc or ridge of extended (∼6″ long) emission immediately to the west (∼1.5″ away). The point source is presumed to be photospheric emission because it has a very faint ($m_G = 20$) optical emission

component (as seen by GAIA) and is not detected in the IRAC 5.8 or 8 μm images, nor at longer wavelengths. In contrast, the arc of infrared emission becomes the only detected emission source at the SOFIA wavelengths, and is most prominent at 20 μm. However, at 37 μm, the infrared arc begins to fade, and in the Herschel 70 and 160 μm images (not shown here), there does not appear to be any detectable emission at this location (from either the stellar source or mid-infrared arc) above the widespread nebular emission of the GH II region. Therefore, the emission seen from 5.8–37.0 μm is likely from a partial shell or external ridge of emission being heated by the nearby star (seen at $\lambda \leqslant 4.5$ μm), and is likely not an internally heated young stellar object (YSO). As can be seen in Figure 4(d), the emission location of the arc moves farther away from the point-source location as the wavelength increases. This is what is expected for an externally heated object. In fact, the 5.8–37.0 μm data points are better fit with a simple blackbody of ∼205 K, than with the YSO SED fitting algorithm, which further implies that the mid-infrared source
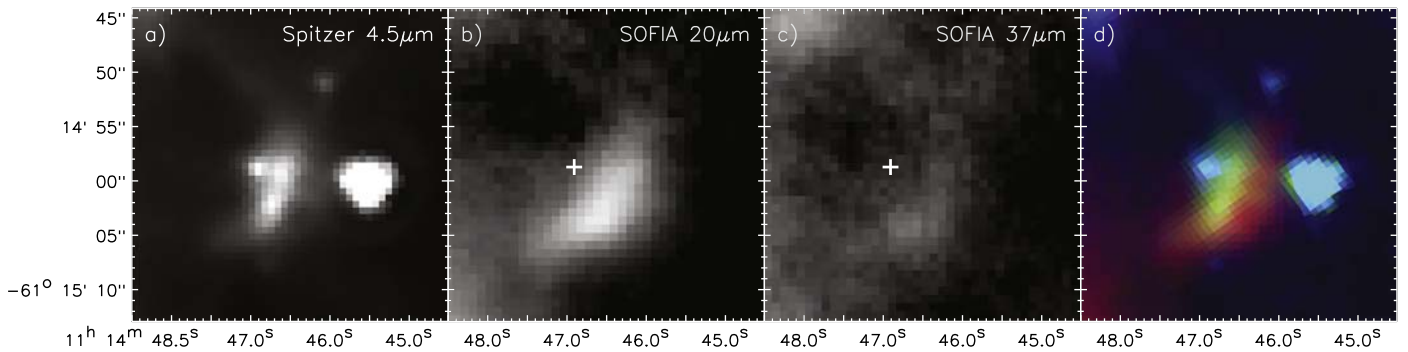
Figure 4. Images of source 1 at (a) Spitzer 4.5 μm, (b) SOFIA 20 μm, and (c) SOFIA 37 μm. In panel (d), the red, green, and blue image contains data from Spitzer 3.6 μm (blue), Spitzer 4.5 μm (green), and SOFIA 20 μm (red). In panels (b) and (c), the white cross marks the location of the near-infrared stellar source closest to (and presumably heating) the mid-infrared dust arc.
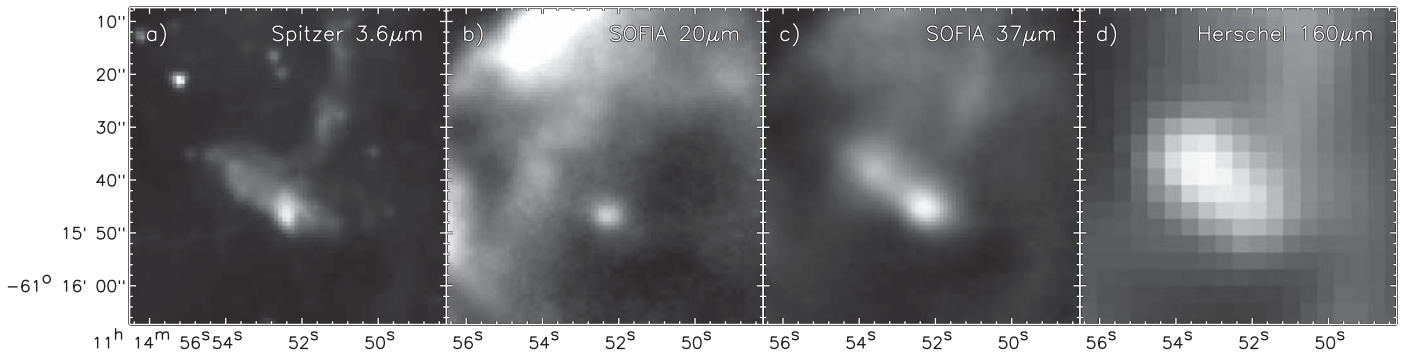

Figure 5. Images of source 2 at (a) Spitzer 3.6 μm, (b) SOFIA 20 μm, (c) SOFIA 37 μm, and (d) Herschel 160 μm. Source 2 is assumed to be the peak seen at 20 μm; however, there may be a second, more deeply embedded source ∼10″ to its northeast (as seen in the 37 and 160 μm images).

seen with SOFIA is likely not a YSO. This region is not covered by either the Nürnberger & Stanke (2003) mid-infrared nor the De Pree et al. (1999) radio continuum maps.

3.1.2. Source 2

Source 2 appears as an elongated bar of emission measuring ∼14″ long running northeast to southwest (p.a. ∼ 300°). In the southwest part of the bar, there is a peak seen at the shorter infrared wavelengths (i.e., from 3.6 to 37 μm), and at 160 μm, the peak switches to the northwest part of the bar (Figure 5). The exception is the 20 μm image where the source appears as a point source (at the southwest location), but there is little to no discernible extended emission (above the extended nebular emission of the GH II region) from the rest of the bar. Furthermore, at 37 μm, the bar appears to have a slight deficit in emission between the northeast to southwest peaks, giving the impression of a double source. This source was not covered by the Nürnberger & Stanke (2003) mid-infrared maps, so we have no higher-resolution observations to confirm or deny this claim. Therefore, there could be a younger and/or more embedded source in the northeast (as evidenced by the rising SED into the far-IR), and an older and/or less embedded source to the southwest (as evidenced by the bright peak seen in the near-IR), which are not completely resolved from each other and together give the impression of a bar of emission. Alternatively, the southwest peak could be the only YSO, and the extended emission is the envelope from which it formed. Because we cannot clearly resolve two sources in the multiwavelength data, we modeled this source as a single source and find it to be well-fit by a range of MYSO models from 16–32 $M_\odot$ with a best-fit mass of 24 $M_\odot$. Interestingly, the

radio continuum maps of De Pree et al. (1999) show no radio emission peak at this location, and therefore, if the object is indeed an MYSO, it must be a very young MYSO prior to the onset of producing significant ionizing radiation.

3.1.3. Source 3 and Radio Source B

Radio continuum region B (De Pree et al. 1999) is a triangular-shaped region whose northern vertex appears to be nearly coincident with source 3. There are infrared ridge structures (best seen at 37 μm in Figure 6) that mimic this triangular shape, and thus, it may be that it is an aspherical compact H II region or ionized cavity. Source 3 itself can be seen in all Spitzer-IRAC bands as a point source with an arc of emission to the north partially surrounding it at a radius of ∼5″ (Figure 6(a)). This appears to be embedded in a larger arc of emission (∼30″ across) that can be seen well at 37 μm and is the only structure that can be seen at 70 μm (Figure 6(d)). Interestingly, this larger arc is not seen at 20 μm, and the point sources at the inner arc are unresolved from each other. In particular, at 70 μm, this arc appears to extend and almost completely surround the radio continuum radio. Given that there is no star seen in the center of the radio continuum region, it may be that the point-source component of source 3 is a revealed ionizing star responsible for the radio continuum emission, and the asymmetry of the ionized region may be due to environmental conditions (i.e., there is denser material to the north). Contrary to this, however, the CS map of Nürnberger et al. (2002) shows that there is a clump here called MM6 whose molecular emission appears to peak south of source 3, between radio sources A and B. This region is not covered by either the Nürnberger & Stanke (2003) mid-infrared maps.
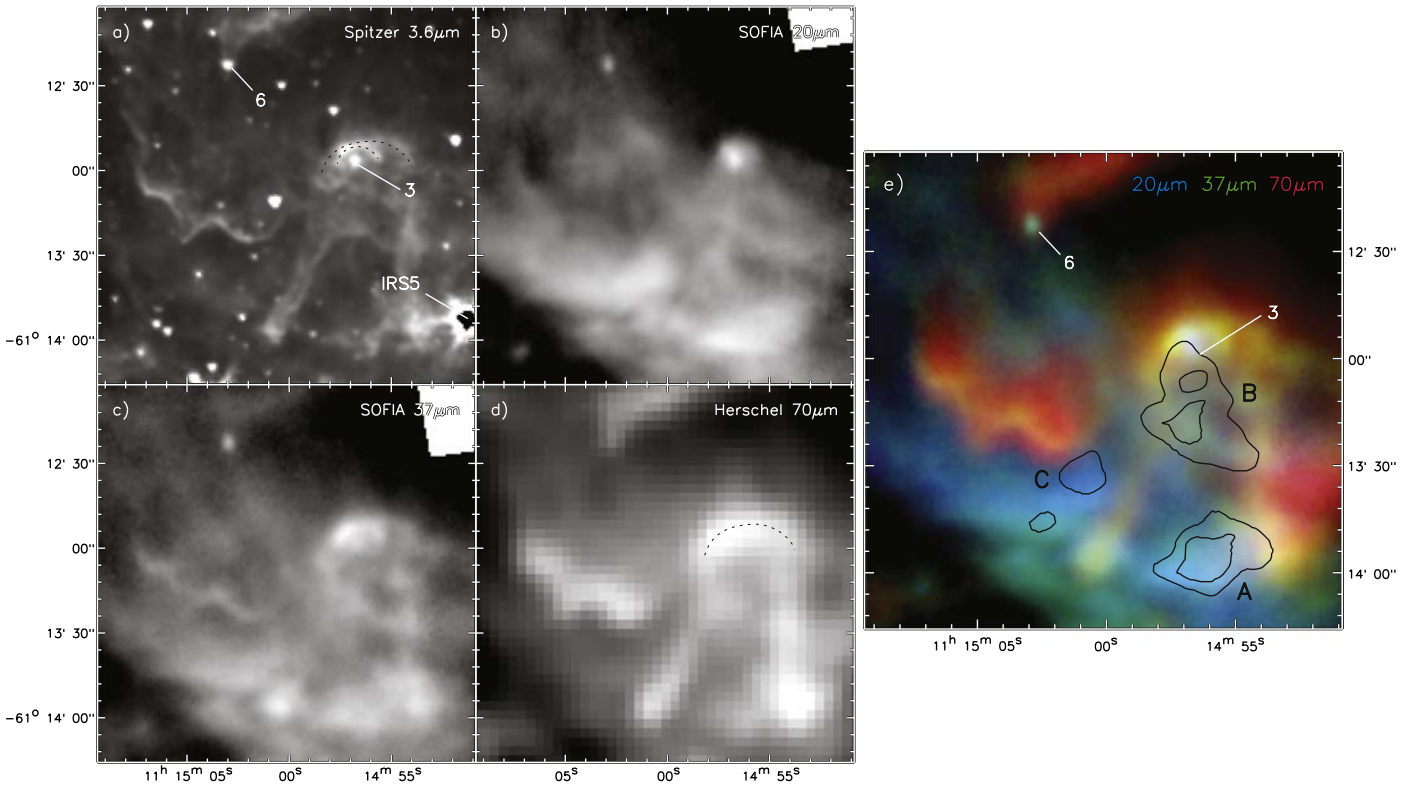
Figure 6. Images of sources 3 and 6 and the radio A, B, and C regions at (a) Spitzer 3.6 μm, (b) SOFIA 20 μm, (c) SOFIA 37 μm, and (d) Herschel 70 μm. In panel (e), the region is shown as a three-color infrared composite with the radio continuum contours of De Pree et al. (1999) overlaid and the major radio regions labeled.
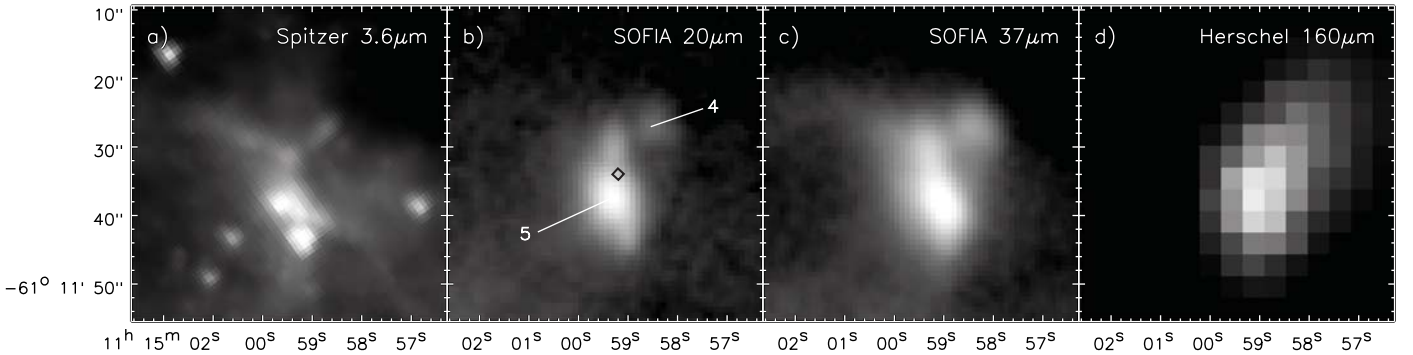

Figure 7. Images of the region containing the sources 4 and 5, at (a) Spitzer 3.6 μm, (b) SOFIA 20 μm, (c) SOFIA 37 μm, and (d) Herschel 160 μm. The black diamond denotes the location of MYSO candidate Her-38 from Di Cecco et al. (2015).

Using photometry obtained by integrating over the combined area of the point source and inner arc at all wavelengths, we find that source 3 is well-fit by a range of MYSO models from 16–24 $M_\odot$ with a best-fit mass of 16 $M_\odot$.

3.1.4. Sources 4 and 5

Sources 4 and 5 are the northernmost compact IR sources on our SOFIA maps. At both 20 and 37 μm, source 5 appears to be elongated north–south, and source 4 appears as a point-like source 12″ to the northwest of the peak of source 5. At shorter infrared wavelengths, the two sources appear to be connected via a ridge of dust emission, and source 5 appears to have a tail toward the northeast (this tail is also seen at 37 μm). Together, the more compact source plus the extended emission appear as a "Y"-shaped morphology in the 3.6–8.0 μm Spitzer images (Figure 7). However, the Spitzer images also reveal that source

5 has two near-infrared peaks, the northern one coincident with the 20 and 37 μm peak. We conjecture that the southern near-infrared peak is a more revealed stellar source as it fades rapidly toward longer wavelengths (i.e., it is completely absent in the 20 μm image), whereas the northern near-infrared peak of source 5 is more embedded as it continues to be the peak in emission all the way out to 160 μm. An MYSO (Her-38) is identified near here by Di Cecco et al. (2015) with coordinates $\sim$3″ from the peak at 37 μm, but looking at the region in the Herschel 160 μm filter (Figure 7), it is likely the same source. Our SED fitting shows source 5 to be best fit by an MYSO model with a mass of 16 $M_\odot$ with a range of MYSO models fits from 16–32 $M_\odot$. Source 4 is very faint in the Spitzer images, but becomes substantially bright enough by 160 μm to be seen as a bright tongue of emission northwest of the peak of source 5. Our SED fitting shows source 4 to be a less-massive YSO

than source 5, with all well-fit MYSO models having a mass of $8\,M_\odot$. Whether or not these MYSOs display any radio continuum emission is unknown, as this region is not covered by the De Pree et al. (1999) radio continuum maps (incidentally, nor was it covered by the Nürnberger & Stanke 2003 mid-infrared maps).

3.1.5. Source 6

Source 6 appears as a point-like source at 20 and 37 μm (Figure 6). However, in the Spitzer images, it can be seen that this mid-infrared peak corresponds to the location of a near-infrared peak that resides at the tip of a photoablated trunk (see Figure 6(a)). This trunk points back toward the HD 97950, and thus, this OB cluster is likely to be responsible for the erosion around this source (as it is for most trunks in the area). At 70 and 160 μm, the dust from the shaft and base of the trunk is more prominent than the dust near the stellar source at the tip. Our SED fitting shows this source is likely to be an MYSO of $8\,M_\odot$. This area is covered by the radio continuum maps of De Pree et al. (1999), but there is no detectable m emission from source 6, indicating that it is likely to be a very youthful MYSO, at a stage prior to the onset of ionized emission.

Since this MYSO is located at the tip of a photoablated trunk, one interesting consequence is that it likely will not be able to continue to accrete much more mass, even though it is a fairly youthful state, due to the fact that its reservoir of material is being stripped away.

3.1.6. IRS 4

IRS 4 was first detected in the 2 μm images of Frogel et al. (1977). This is a bright stellar source that can be seen readily in the optical ($m = 12$ in the GAIA G passband) but is considered to be a long-period variable candidate (Gaia Collaboration 2020). It is the brightest stellar object in all of NGC 3603 at Two Micron All Sky Survey (2MASS) J band ($m_J = 6.7$; Cutri et al. 2003), but it decreases in flux quickly with increased wavelength. It is saturated in all Spitzer-IRAC bands (not shown here). It is clearly detected in the higher angular resolution 12 μm map of Nürnberger & Stanke (2003), and also appears as a prominent point source at 20 μm (Figure 2), but is just barely detected at 37 μm (Figure 3), and it is not detected at 70 or 160 μm (not shown here). Given the behavior of flux as a function of wavelength alone (as well as the lack of a radio continuum component, e.g., De Pree et al. 1999), it can be concluded that this is likely to be a (perhaps almost) completely revealed stellar source, and the flux measured at all wavelengths is likely to be predominantly photospheric emission. Indeed, based upon the measured near-infrared colors, Frogel et al. (1977) claim IRS 4 is an M supergiant. Although Frogel et al. (1977) conjecture the source is likely to be at the distance of NGC 3603, the GAIA parallax measurements for this source place it at 3433 ± 28 pc. Therefore, since NGC 3603 is at 7.2 kpc, this source is a foreground stellar source. Given the above information, and the fact that we only have one nominal flux data point (i.e., at 20 μm), we did not attempt to use the MYSO SED fitter on this source.

3.1.7. Source 7

This source is overall a faint object, appearing brightest in the SOFIA 20 μm image (Figure 2). It is barely visible in the Spitzer 3.6 μm image, and it is not detected in the Herschel 70 or 160 μm images (not shown here). It is identified as source

5A in the 12 μm map of Nürnberger & Stanke (2003), but we do not see in the SOFIA data any hints of sources 5B or 5C.[6] Our SED of this source appears to turn over near 20 μm, and the MYSO fitter does a poor job of fitting the data. We find that a simple blackbody of $\sim$220 K fits the SED better, and therefore, we believe that this source is a knot of dust and not an internally heated YSO.

3.1.8. Source 8

In the Spitzer 3.6–8.0 μm images (not shown here), this source appears as a point-like source located in (or in projection against) a large ($\sim$0.′9) ridge of dust running more or less east–west. A compact source is detected at 20 μm (Figure 2) and at 37 μm (Figure 3); however, at 37 μm, there is more nearby extended nebular emission from the ridge of dust making the source appear less-prominent than at 20 μm. In fact, the ridge of dust is not detected at 20 μm, even though it can be readily seen at all other infrared wavelengths. Although the infrared SED of source 8 is well-fit by a range of MYSO models from 8–$16\,M_\odot$ with a best-fit mass of $8\,M_\odot$, there appears to be no radio continuum emission present here (De Pree et al. 1999). This means this source is likely a youthful MYSO, prior to the onset of significant ionizing emission.

3.1.9. Source 9

This is another source that is compact and bright in the Spitzer-IRAC data (not shown here). It appears as an unresolved source (identified as source 11) in the 12 μm map of Nürnberger & Stanke (2003). It is detected as a compact source at both 20 μm (Figure 2) and 37 μm (Figure 3), but it is not detected above the bright background of the extended nebular dust emission in the Herschel data (not shown here). Our SED fitting show it to likely be an MYSO of $12\,M_\odot$. Once again, there appears to be no radio continuum emission present here (De Pree et al. 1999), and therefore, source 9 is likely to be an MYSO in the earliest stages of development.

3.1.10. IRS 9

This source is the brightest compact source on the entire NGC 3603 field at both 20 and 37 μm (see Figure 8). First detected by Frogel et al. (1977), it can also be seen in the 12 and 18 μm maps of Nürnberger & Stanke (2003). While the source appears elongated to the northwest in the SOFIA data, this is the direction the telescope was chopping, and this elongation is therefore not intrinsic to the source but due to problems with the stability of the chopping mechanism during these observations (see discussion in Section 2). There are two additional infrared point sources located west of the main IRS 9 peak, as first detected in the higher angular resolution 12 and 18 μm data of Nürnberger & Stanke (2003), Nürnberger (2003), and seen in the Spitzer data (Figure 8(a)). Those authors call the main bright point source IRS 9A (coincident with the SOFIA 20 and 37 μm peak), and the fainter sources IRS 9B and IRS 9C. IRS 9B and IRS C are not seen in the SOFIA images (Figures 8(b) and (c)), and the peak seen at both 70 and 160 μm is coincident with the location of IRS 9A (Figure 8(d)). IRS 9B and IRS 9C have optical emission as seen with GAIA, as does IRS 9A (DR3 5337417774995179776;

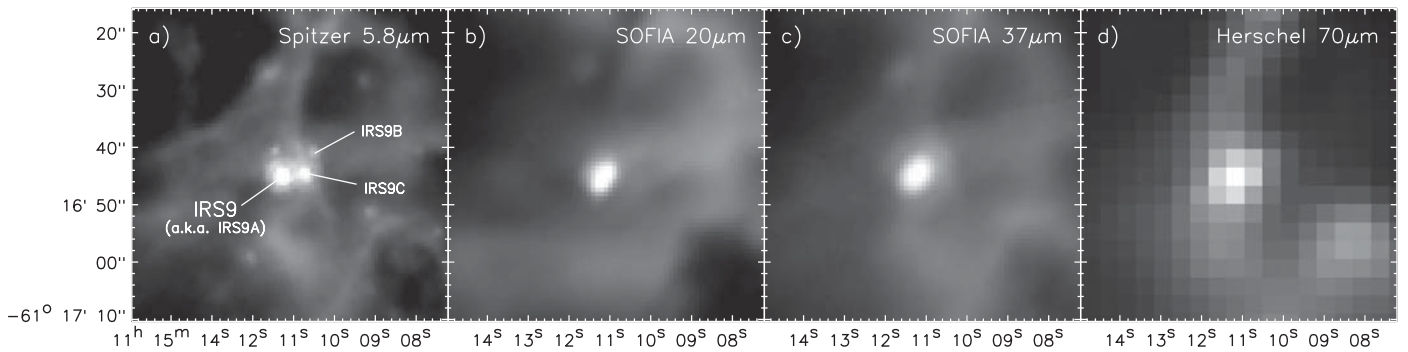[6] In the SOFIA data, we furthermore only see the nearby components 16A and 16B, barely, at 20 μm.

Figure 8. Images of the region containing IRS 9, at (a) Spitzer 5.8 μm, (b) SOFIA 20 μm, (c) SOFIA 37 μm, and (d) Herschel 70 μm. The source appears artificially elongated in the SOFIA images due to telescope issues during the observations.
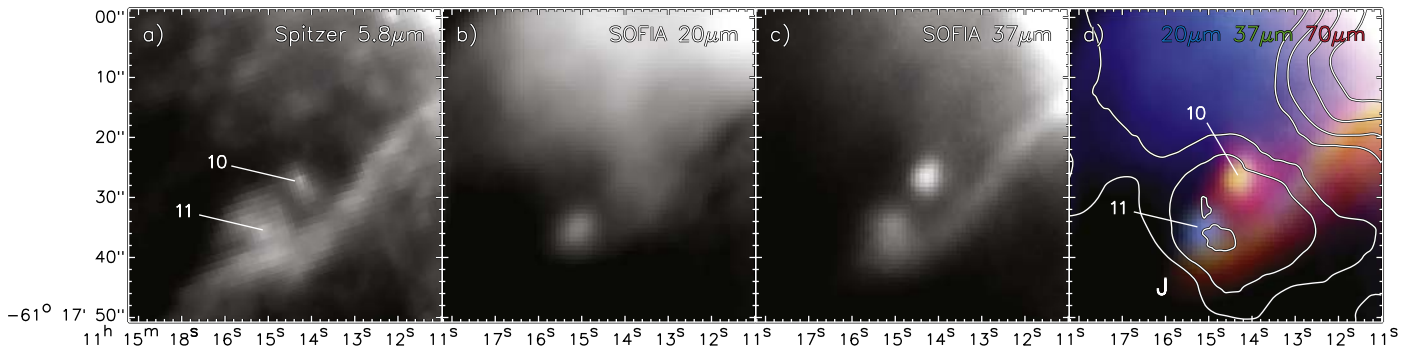

Figure 9. Images of the region containing sources 10 and 11 and radio continuum peak J, with (a) Spitzer 5.8 μm, (b) SOFIA 20 μm, and (c) SOFIA 37 μm. In panel (d), the region is shown as a three-color infrared composite with the radio continuum contours of source J from De Pree et al. (1999) overlaid and labeled.

$m_G \sim 17$); though, no distance determination is listed in that catalog for any of the sources.

Despite the prominence of IRS 9A across the entire infrared, it lacks detectable radio continuum emission. Although extended radio continuum emission does go through the area of this source, it has no peak located here. Frogel et al. (1977) claim that it is the reddest point source on the field and thus must be surrounded by significant dust, and therefore, it is likely to reside within NGC 3603. Our SED modeling shows this source is well-fit by a range of MYSO models from 32–64 $M_\odot$ with a best-fit mass of 64 $M_\odot$, and this is the source with the highest mass found in all of the sources we modeled. Given the lack of prominent radio continuum emission, this MYSO must also be very youthful. Given the fact that there is also a optical component seen, this may mean that the source is situated with its outflow axis pointing toward us.

3.1.11. Sources 10 and 11

Sources 10 and 11 are separated by only $\sim$11", and both lie within the confines of the radio region J defined by De Pree et al. (1999). They both also lie just to the north of a ridge of emission, best seen in the Spitzer-IRAC bands (Figure 9).

Source 10 is coincident with water maser emission (Caswell et al. 1989). It is barely visible in the Spitzer 3.6 μm image but brightens at longer IRAC wavelengths, and becomes more prominent than source 11 in our 37 μm and longer infrared wavelength data (Figure 9). Using Herschel data, Di Cecco et al. (2015), who identify this source as Her-83, showed that the source is well-fit by MYSO SED models. Interestingly, it is not seen in the 12 μm maps of Nürnberger & Stanke (2003), and a peak is not detectable here in the SOFIA 20 μm maps above the extended nebular emission either (Figure 9(b)).

Nonetheless, our SED modeling shows good fits for a stellar mass of 16 $M_\odot$, but we caution that there is only one nominal data point used in the fit beyond 8 μm (i.e., 37 μm), so this result is less trustworthy.

Source 11 is coincident with a 12 μm unresolved point source in the images of Nürnberger & Stanke (2003), which they call source 10. The mid-infrared emission can be seen at this location out to 37 μm (Figure 9), but is not detectable as a source at Herschel 70 and 160 μm above the emission from the ridge of dust present here. The infrared peak of source 11 also appears to have an optical component ($m = 12$ in the GAIA G passband), and in the Spitzer-IRAC 5.8 (Figure 9(a)) and 8.0 μm images, it is surrounded almost entirely by a dust shell with a radius of $\sim$4". At the longer SOFIA wavelengths, there is not sufficient resolution to separate the point source and shell emission, and so, our photometry of this source includes an area covering both the point source and shell.

Confusingly, the GAIA optical source found here (which has a position that agrees with the infrared peak to within 1") has a distance of only 553 $\pm$ 5 pc. However, from the infrared fluxes of this source, we find an SED that is best fit by an MYSO model of 16 $M_\odot$, with good fits ranging from 16–24 $M_\odot$. Furthermore, the peak of the extended radio continuum source J peaks very close to the infrared peak of source 11 (see Figures 2 and 3). It may be that the optical point-source component and the more extended infrared component are simply a chance alignment of a field star and an MYSO, and are unrelated to each other.

3.1.12. Source 12

This source is a very bright unresolved point source in the near-infrared, so much so that it is completely saturated at all
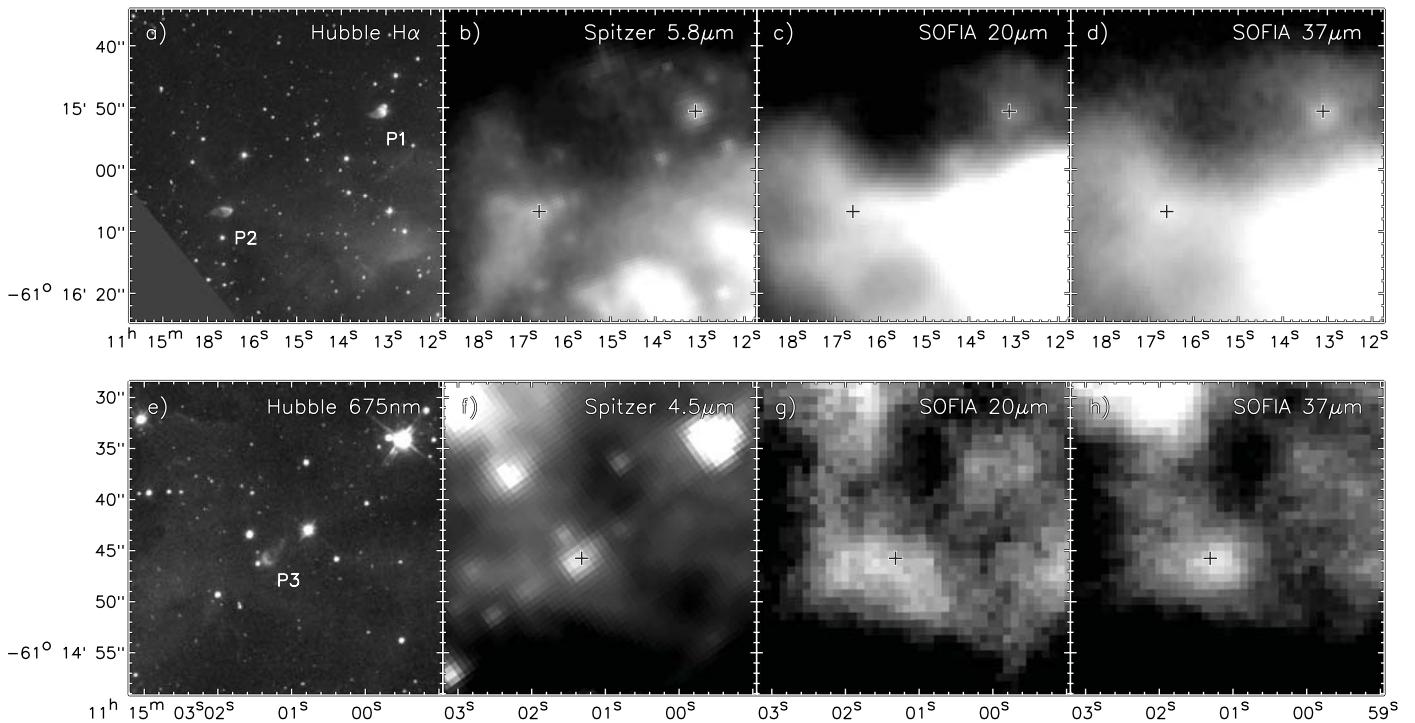
Figure 10. Images of the regions containing the proplyd sources P1 and P2 (top row) and P3 (bottom row). Panels (a) and (e) show Hubble images, panels (b) and (f) show Spitzer-IRAC images, panels (c) and (g) show the SOFIA 20 μm images, and panels (d) and (g) show the SOFIA 37 μm images. The proplyds are labeled in the Hubble images, and their positions are given by the crosses in all other images. SOFIA images were shifted by one pixel ($0\farcs768$) in R.A. to better align to the Hubble data.

Spitzer-IRAC wavelengths (not shown here). Although it is well-detected at 20 μm (Figure 2), it is barely detected at 37 μm (Figure 3), and not visible in either of the 70 or 160 μm Herschel passbands (not shown here). Given that there are only two photometry points for this source (20 and 37 μm), and that the flux decreases substantially from 20 to 37 μm, we suggest that this source is an evolved (main-sequence) star and not a YSO. Indeed, it does have an optical component, and although observed with GAIA (DR3 5337418221666129792), it is rather faint ($m_G = 18.5$) and highly variable with no accurate distance derivation given in the GAIA catalog. Like IRS 4, given the obvious stellar nature of this source and the lack of data points, we did not attempt to model this source with the MYSO SED fitter.

3.1.13. Radio Source F

There is an infrared peak seen in the SOFIA 20 and 37 μm images (see Figures 2 and 3) that aligns well with the radio continuum peak labeled source F by De Pree et al. (1999). Radio peak F is embedded in a larger extended radio continuum emission region, and it is unclear if it is a YSO itself, or just an ionized knot of dust. Although no clear peak can be seen here at 70 or 160 μm, there is an obvious knot of emission seen in the extended dust in this area in the Spitzer-IRAC data at all wavelengths. The SED fitting algorithm best fits this source as a 16 $M_\odot$ MYSO; however, the fit is poor, raising some doubt as to its true nature.

3.1.14. The Proplyds: P1, P2, and P3

Based upon HST/WFPC2 observations in the optical and Very Large Telescope/ISAAC observations in the near-infrared, Brandner et al. (2000) discovered three tadpole or cometary shaped objects within NGC 3603, possessing ionization fronts at their heads, which face the HD 97590 stellar cluster, and ionized tails pointing away from the cluster. It is claimed by Brandner et al. (2000) that these structures are analogous to the proto planetary disks (proplyds) seen in Orion (O'Dell et al. 1993); though, they are 20 to 30 times larger in size.

There exists some diffuse 12 μm emission in vicinity of P1 as seen by Nürnberger & Stanke (2003). In our SOFIA 20 and 37 μm images, we definitively see a peak a the location of P1 at both wavelengths (Figures 10(c) and (d)), and it is clearly detected at all Spitzer-IRAC bands (e.g., Figure 10(b)). Even in the Herschel 70 and 160 μm images, there appears to be a tongue of faint emission extending out (but only partially resolved) from the bright infrared emission region associated with radio source E. Attempting to do the best we could to isolate emission just from P1, we performed SED fitting to the photometry of the source and find that it is well-fit by several MYSO models all having a mass of 8 $M_\odot$.

Although there is a weak peak seen at the location of P2 in all infrared wavelengths from 3.6–160 μm, as Nürnberger & Stanke (2003) point out, at most of these wavelengths, the emission from a ridge of dust extended through here that makes it difficult to isolate the flux from just the proplyd itself at most wavelengths. The exception to this is the 70 μm Herschel images, where P2 seems to be a point-like source at these wavelengths. Again, we isolated the emission from just P2 at all wavelengths as best as we could, and we were able to use the SED fitter to fit the data with a range of MYSO models from 12–32 $M_\odot$ with a best-fit mass of 12 $M_\odot$.

Proplyd P3 is clearly seen at all Spitzer-IRAC wavelengths (e.g., Figure 10(f)); though, at 8 μm, there are significant array artifacts that make the data unusable for photometry). The

higher angular 12 μm images of Nürnberger & Stanke (2003) show a faint detection of emission at the location of P3. In the SOFIA data, there exists a diffuse region of emission at this location with a broad peak near P3 at 20 μm (Figure 10(g)), and a more definitive detection of a peak at 37 μm (Figure 10(h)). At 70 and 160 μm, there appears to be a peak here as well, but like the SOFIA data, it is not fully resolved from nearby extended emission features. Again, isolating the flux from just P3, we found the fluxes were well-fit by a range of MYSO models from 8 to 16 $M_\odot$ with a best-fit mass of 12 $M_\odot$; however, this fit is only based upon 2 nominal data points (and 5 upper limits).

At a minimum, the detection of infrared emission at thermal infrared wavelengths for all three sources (although varied in their strength) indicates that these sources indeed possess circumstellar dust of some kind. Our SED modeling shows that these sources may indeed be legitimate MYSOs, and therefore may possess not only circumstellar disks (like proplyds), but they are likely to also be surrounded by dust envelopes as well. These results seem to contradict the speculations by Nürnberger & Stanke (2003) that these sources may be small, denser clumps of gas that have simply not yet been photoevaporated away by the OB stars present in NGC 3603, constituting the last remnants of environmental overdensities present in the original molecular cloud. Furthermore, proplyds can be confused with cometary-shaped ultra-compact H II (UCH II) regions, with the main distinction being that proplyds are externally ionized, whereas UCH II regions have a central massive star responsible for ionizing the structure internally. The results of the radio study by Mücke et al. (2002) showed that the radio flux of the proplyds in NGC 3603 could be entirely attributed to external ionization by the HD 97590 stellar cluster alone, and they speculate that it is unlikely that any central stars to these sources would be $>10 M_\odot$. However, our conclusions are that these objects may indeed contain YSOs massive enough to ionize their surroundings, and thus, it is unclear if these are genuine proplypds or cometary UCH II regions.

3.1.15. Sher 25

Located about $20''$ north of the HD 97950 star cluster, Sher 25 is an evolved blue supergiant (BSG), discovered by Sher (1965) at optical wavelengths and later spectral typed by Moffat (1983) to be a B1.5 Iab star. Brandner et al. (1997b) discovered the BSG is surrounded by a circumstellar ring with a diameter of $\sim$0.4 pc and detect what they believe are bipolar outflow clouds located northeast and southwest on the ring separated $\sim$20 pc from the central star.

The clumpy circumstellar ring structure and bipolar clouds are best seen in the HST images of Brandner et al. (2000), especially in the Hα filter (Figure 11(e)). Our SOFIA 20 μm map shows dust emission present around the entire circumstellar ring, and also shows faint emission from the East Cloud (to use the nomenclature of Hendry et al. 2008) of the bipolar clouds (Figure 11(a)). The emission from the circumstellar ring is enhanced substantially in the northwest and southeast ends of the ring, which would be expected for a ring tilted to our line of sight (i.e., 64° against the plane of the sky, and with a position angle of $\sim$165°, as measured by Brandner et al. 1997b) as the pathlength of dust (and hence quantity of emitting material) is larger at these locations. With that being said, as seen in Figure 11(b), our deconvolved 20 μm SOFIA image shows clumpy structures colocated with the clumps seen in the Hubble Hα image (Figure 11(e)). The SOFIA 37 μm image

shows dust emission mostly from the northwest and southeast ends of the ring, but both the East and West Clouds are well-detected (Figure 11(d)). Figure 11(f) shows the good spatial correlation between the structures seen in the SOFIA images and the Hubble Hα images. In the circumstellar ring, the SOFIA clumps are seen to be colocated with the Hα clumps, and the emission at 37 μm forms the East and West Clouds that can be seen to align well with the structures seen in the Hubble image as well.

The only dust emission seen in the Spitzer 3.6 μm image is from the East Cloud (and the BSG is also apparent at this wavelength as well as all other Spitzer-IRAC wavelengths). Emission from both clouds and the circumstellar ring are evident in the Spitzer images at 4.5, 5.8, and 8.0 μm. At Herschel 70 μm, emission can be seen coming from all three objects as well, but at 160 μm, the Clouds are more apparent than the emission from the ring. From this behavior of flux as a function of wavelength alone, it can be ascertained that the dust emission in the Clouds is cooler than the dust in the ring.

It was hypothesized by Brandner et al. (1997a) that the East and West Clouds are part of a hourglass-shaped circumstellar nebula, and that the hourglass nebula and ring are akin to similar structures seen around SN 1987A, which were believed to have been created by its supergiant progenitor star prior to going supernova. Hubble images by Burrows et al. (1995) showed that the hourglass-shaped nebula around SN 1987A is best seen in narrowband Hα images. Such a hourglass-shaped nebula is not readily apparent in the Hubble Hα image in Figure 11(e); however, Brandner et al. (1997a) showed that there is some (less-compelling) evidence in their Hubble near-infrared spectroscopic channel maps, which show a hint of a broken outline of an hourglass structure seen in the Hα line. Perhaps lending credence to the existence of this structure, our SOFIA image at 20 μm shows emission outlining the entire hourglass-shaped nebula (see red dashed ellipses in Figure 11(c)), although the northeastern lobe appears to be filled in more with infrared emission than the southwestern lobe.

Sher 25 is optically bright enough that it is included in the GAIA Data Release 3 (DR3) catalog. Based upon parallax measurements, Sher 25 is located at 5873^{+30}_{-102} pc, placing it in the foreground of NGC 3603 by more than a kiloparsec. As the distance to NGC 3603 was also determined using GAIA (second data release, hereafter DR2) parallaxes, this means that Sher 25 is unlikely to be directly associated with the star-forming activity of NGC 3603. A similar conclusion was recently made by Weßmayer et al. (2023) using distances derived from both GAIA data and spectrophotometric techniques.

3.1.16. IRS Sources from Frogel et al. (1977)

The coordinates of IRS 1 and IRS 2 define the peaks seen in the low-resolution 10 and 20 μm images of Frogel et al. (1977). These correspond to the brightest mid-infrared emission we see in the SOFIA data centered roughly on the peaks of radio sources E and H, respectively. IRS 3 also is defined in that same paper by a structure in the 10 μm image, which appears as a tongue of emission toward the west of IRS 1. While there is extended emission present here at all higher-resolution near-infrared, as well as mid-infrared and far-infrared images, there is nothing that could be identified as a peak or separate region (Figures 2 and 3).

The rest of the sources (i.e., IRS 4–IRS9 and IRS 12–IRS 15; there are no IRS 10 or IRS 11) are defined by the 2 μm data of
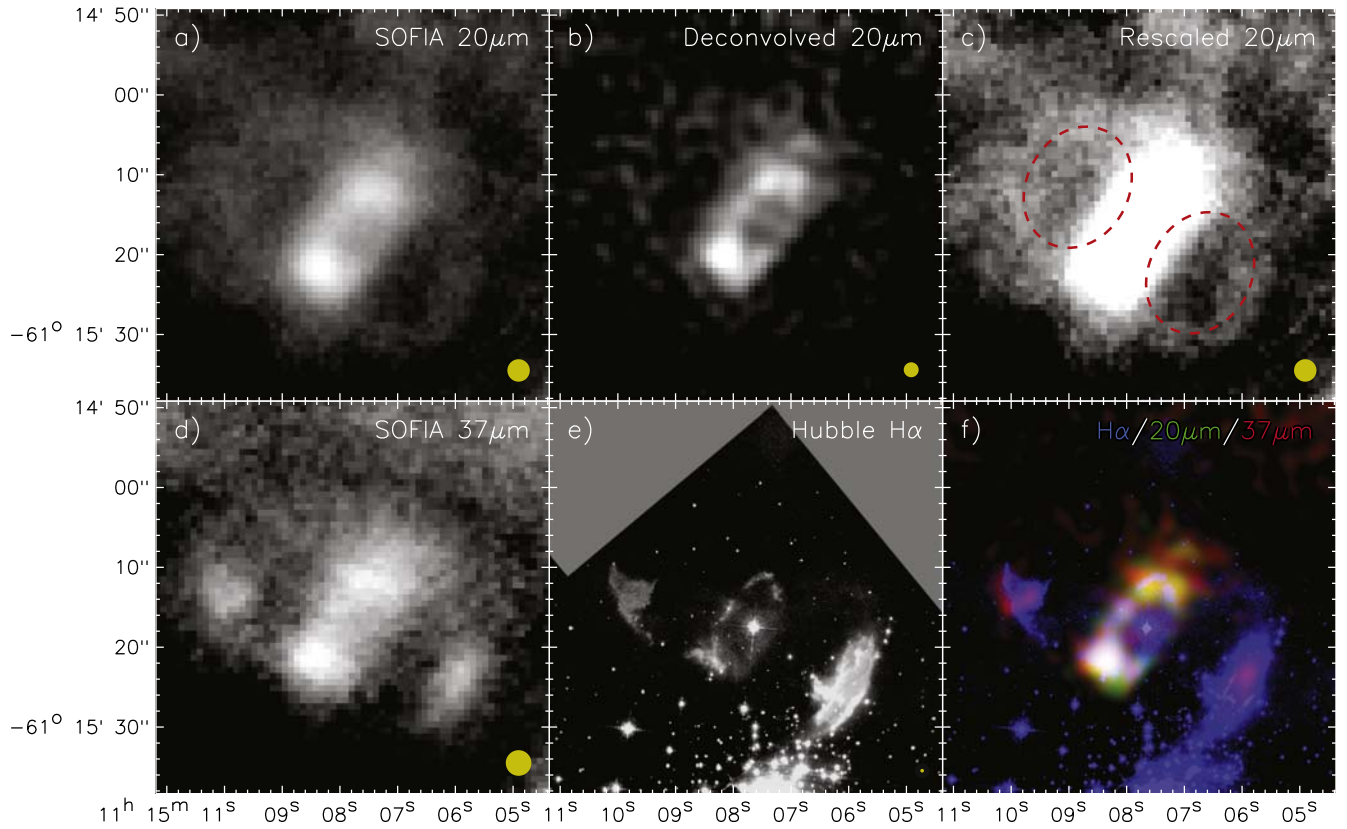
Figure 11. Images of circumstellar ring and hourglass nebula of Sher 25. (a) The 20 μm by SOFIA. (b) The deconvolved 20 μm SOFIA image showing the clumpy dust structures within the circumstellar ring. (c) The 20 μm by SOFIA rescaled to show the fainter emission from the hourglass nebula (traced by the dotted red lines). (d) The 37 μm by SOFIA. (e) The Hubble Hα image. (f) A three-color image made from the Hubble Hα image (blue), the SOFIA deconvolved 20 μm image (green), and the SOFIA deconvolved 37 μm image (red). The yellow filled circles in the lower right corner of panels (a)–(e) indicate the resolution of the image at the given wavelength.

Table 1
Updated Coordinates and Distances of the Near-infrared IRS Sources in NGC 3603

Source	R.A. (J2000)	Decl. (J2000)	Dist.[a] (pc)	GAIA DR3 ID
IRS 4	11:15:03.62	−61:14:22.3	3433^{+28}_{-28}	5337418462189917952
IRS 5	11:14:51.31	−61:13:52.6	4914^{+12}_{-30}	5337421043475869184
IRS 6	11:15:25.91	−61:13:41.8	8022^{+378}_{-936}	5337419772188803712
IRS 7	11:14:59.25	−61:19:28.4	5833^{+70}_{-48}	5337042399168099072
IRS 8[b]	11:15:08.93	−61:16:00.4	4274^{+54}_{-94}	5337418015513337472
IRS 9	11:15:11.38	−61:16:45.2	...	5337417774995179776
IRS 12	11:14:58.28	−61:17:17.5	2866^{+91}_{-111}	5337417912434087680
IRS 13	11:14:54.00	−61:18:35.4	...	5337042570966803328
IRS 15	11:15:25.24	−61:12:01.5	...	5337419905291591296

Notes. These are updated coordinates for the near-infrared sources given by Frogel et al. (1977). New centroid data are from the closest bright source seen in the 2MASS 2 μm data. No clear near-infrared source can be found for IRS 14, and there are no IRS 10 or IRS 11 coordinates tabulated in Frogel et al. (1977) as they were too faint.

[a] Distances are from the GAIA Data Release 3 (DR3) catalog and determined from parallax measurements. The distances to IRS 9, IRS 13, and IRS 15 are not given in the catalog.

[b] IRS 8 has two sources within the original ∼10″ source position error. The coordinates and information are for the brightest of the two sources. The fainter source is GAIA DR3 5337418015513340160 and is located 5″ southwest of this source and has no GAIA-determined distance.

Frogel et al. (1977). Of these near-infrared-defined sources, only IRS 14 does not have an obvious source in the Spitzer data or 2MASS data, while the rest have clearly visible and bright Spitzer-IRAC sources (usually saturated) and 2MASS 2 μm sources, too, within the quoted 10″ astrometric accuracy. In our figures in this paper (best seen in Figures 2 and 3), we have identified and labeled the locations of the 2MASS sources we

believe to be associated with each IRS source, and have tabulated the centroids based upon the 2MASS 2 μm data in Table 1. IRS 4 and IRS 9 are the only near-infrared-defined sources with emission peaks seen in our SOFIA data.

We have also searched for each of these sources in the GAIA DR3 catalog, and indeed, all are found to have an optical counterpart within 1″ of their near-infrared peak positions

Table 2
SOFIA Observational Parameters of Compact Sources in NGC 3603

Source	R.A. (J2000)	Decl. (J2000)	20 μm			37 μm			Aliases
			R_{int} (arcsec)	F_{int} (Jy)	F_{int-bg} (Jy)	R_{int} (arcsec)	F_{int} (Jy)	F_{int-bg} (Jy)	
1	11:14:46.42	−61:15:02.2	10	43.2	20.2	9.2	41.9	30.4	⋯
2	11:14:52.27	−61:15:46.8	6.9	31.5	9.21	9.2	184	73.1	⋯
3	11:14:56.76	−61:12:55.5	12	142	54.9	13	548	241	⋯
4	11:14:58.36	−61:11:26.4	4.6	5.24	2.81	4.6	40.5	23.4	⋯
5	11:14:59.31	−61:11:37.2	11	88.9	75.0	12	408	317	⋯
6	11:15:02.92	−61:12:21.7	5.4	19.2	5.01	6.1	62.2	15.6	⋯
7	11:15:03.77	−61:15:05.3	6.9	18.6	6.00	5.4	15.2	2.18	[NS03] 5A
8	11:15:07.28	−61:14:04.7	6.9	16.8	5.35	8.4	81.7	17.4	⋯
9	11:15:10.16	−61:17:37.4	6.9	49.7	7.21	7.7	188	45.3	[NS03] 11
10	11:15:14.28	−61:17:26.2	5.4	42.7	⋯	5.4	118	14.8	Her-83
11	11:15:15.28	−61:17:36.6	7.7	65.3	20.6	9.2	256	106	[NS03] 10
12	11:15:16.54	−61:15:01.5	6.1	15.6	10.6	6.1	8.89	2.34	⋯
IRS 4	11:15:03.45	−61:14:22.3	5.4	18.2	9.33	5.4	32.2	⋯	Her-55
IRS 9	11:15:11.22	−61:16:45.2	5.4	218	110	7.7	721	324	⋯
F	11:15:05.15	−61:16:38.3	7.7	212	62.7	9.2	383	91.6	⋯
P1	11:15:12.93	−61:15:49.1	6.9	36.5	4.10	8.4	64.6	23.5	⋯
P2	11:15:16.73	−61:16:06.3	9.2	89.3	⋯	9.2	148	45.9	⋯
P3	11:15:01.29	−61:14:46.5	9.2	38.1	⋯	9.2	95.5	18.3	⋯

Note. If there is no F_{int-bg} value for a source, then the source is not well resolved from other nearby sources and/or extended emission. For these sources, the F_{int} value is used as the upper limit in the SED modeling. For sources with alias names, those prefixed with "[NS03]" are from Nürnberger & Stanke (2003), and those with "Her-" are from Di Cecco et al. (2015).

(i.e., coincident to within our infrared positional measurement uncertainty). The DR3 identification numbers for each IRS source are given in Table 1, along with their distances derived from their measured GAIA parallaxes, as given in the DR3 catalog. IRS 9, IRS 13, and IRS 15 do have optical components, but accurate distances were unavailable in the catalog.

It can be seen from the distances in Table 1 that most of the IRS sources with GAIA distances are not physically associated with NGC 3603. Most appear to be foreground stars, with the exception of IRS 6. At 8022^{+378}_{-936} pc, this source lies at the same distance as NGC 3603 (∼7.2 kpc) to within the errors.

4. Results and Data Analysis

We subdivide the resolved sources of infrared emission within NGC 3603 into compact or extended subregions. The two categories denote which objects we believe are star-forming cores (compact sources) versus the larger star-forming molecular clumps (extended subregions). For the compact sources, we will apply SED models to their multiwavelength photometry to estimate their physical characteristics and to determine which sources are likely to be MYSOs. For the extended subregions, we will estimate their relative evolutionary states using analyses based upon their derived infrared mass, luminosity, and gas kinematics to discern information about the evolutionary state of NGC 3603.

4.1. Physical Properties of Compact Sources: SED Model Fitting and Determining MYSO Candidates

We define a compact source as one that has a definitive peak that does not change location significantly with wavelength, and it must also be detected at more than one wavelength. As was the case in our previous papers, the compact sources chosen have physical sizes ≲0.3 pc, which is consistent with the size of molecular cores, which are on the order of ∼0.1 pc

(Zinnecker & Yorke 2007). We measured flux densities for all compact sources and subregions that could be identified in the SOFIA 20 and 37 μm data. We additionally downloaded Spitzer-IRAC (i.e., 3.6, 4.5, 5.8, 8.0 μm) imaging data and Herschel-PACS (i.e., 70 and 160 μm) imaging data from their respective online archives and measured fluxes for these same sources at all wavelengths. Table 2 contains the information regarding the position, radius employed for aperture photometry, and background-subtracted flux densities measured at both SOFIA wavelengths for all compact sources (and similar information regarding photometry from the Spitzer and Herschel data can be found in Appendix C). We employed the same optimal extraction technique as in Paper I to find the optimal aperture to use for photometry. Background subtraction was also performed in the same way as Paper I (i.e., using background statistics from an annulus outside the optimal extraction radius, which had the least environmental contamination).

We found eighteen compact sources in the SOFIA data, and eight are newly identified here. Using the centimeter radio continuum maps of De Pree et al. (1999), and archival ATCA 6 cm data that are available at similar resolution but with slightly different field coverage, we find that most of these infrared compact sources (14/18) do not correspond to centimeter radio continuum peaks or compact sources. Three of the compact sources are the previously identified proplyds, which are known to have centimeter radio continuum emission from the study of Mücke et al. (2002). The only other compact infrared object with detected centimeter radio continuum emission is radio source F (De Pree et al. 1999). However, most of the infrared compact sources are found to lie embedded within areas of diffuse and extended radio continuum emission, with the exception of sources 6, 7, 8, and IRS 4 where there is no coincident or environmental radio emission detected at all. Sources 4 and 5 are not covered by the De Pree et al. (1999) or
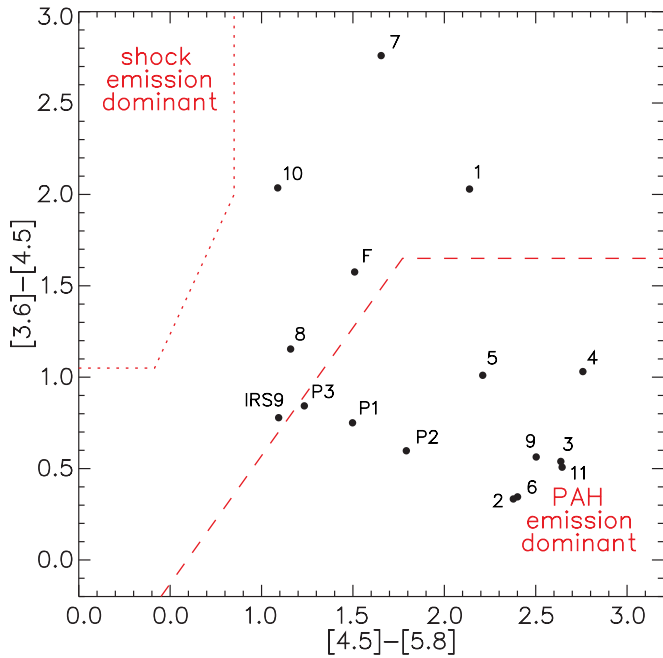
Figure 12. A color–color diagram utilizing our background-subtracted Spitzer-IRAC 3.6, 4.5, and 5.8 μm source photometry to distinguish "shocked emission dominant" and "PAH emission dominant" YSO candidates from our list of compact sources. Above (upper left) of dotted line indicates shock emission dominant regime. Below (bottom right) dashed line indicates PAH dominant regime. We adopt this metric from Gutermuth et al. (2009). Some sources are not included in this diagram due to nondetection or saturation in the Spitzer-IRAC bands.

archival 6 cm maps, and so, whether or not they have associated radio continuum emission peaks is unknown.

Most radio-defined sources from De Pree et al. (1999) are found to be associated with mid-infrared peaks or with enhanced mid-infrared emission regions. The exceptions are radio sources K, L, and M, which lie within extended and diffuse areas of infrared emission but are not associated with any infrared peak or particularly bright infrared regions.

Using the SOFIA, Spitzer, and Herschel photometry, SEDs were constructed for all compact sources, except IRS 4 and source 12. These two sources are saturated in all of the Spitzer wavelengths and are not detected in the Herschel filters, and thus only have two nominal flux values (at 20 and 37 μm). As discussed in Paper I, a color–color diagram using Spitzer-IRAC data (3.6–4.5 μm versus 4.5–5.8 μm) can be used to determine if sources are highly contaminated by shock emission and/or polycyclic aromatic hydrocarbon (PAH) emission, and we have employed that technique here again for the compact sources in NGC 3603. From Figure 12, we see that there are no sources classified as "shock emission dominated"; however, there are a fair number of "PAH emission dominated" sources. For the sources in this latter category, their 3.6, 5.8, and 8.0 μm IRAC fluxes are set as upper limits to the photometry used in constructing the SEDs. Additionally, the Herschel 70 and 160 μm fluxes are set to be upper limits in the SEDs for most sources due to the coarser spatial resolution ($\sim$10″) of the data and the high likelihood that the photometry is contaminated by emission from adjacent sources or the extended dusty environment of NGC 3603.

As we did in Paper I, we set the upper error bar on our photometry as the subtracted background flux value (since background subtraction can be highly variable but never larger

than the amount being subtracted), and the lower error bar values for all sources come from the average total photometric error at each wavelength (as discussed in Section 2 and Paper I), which are set to be the estimated photometric errors of 20%, 15%, and 10% for 4.5, 20, and 37 μm bands, respectively. We assume that the photometric errors of the Spitzer-IRAC 3.6, 5.8, and 8.0 μm fluxes are 20% for the sources that are not contaminated by PAH features. Also, as in Paper I, the error bars of the Herschel 70 and 160 μm data points are assumed to be 40% and 30%, respectively.

Once SEDs were constructed from the photometric data (and their associated errors or limits), we utilized the Zhang–Tan (ZT; Zhang & Tan 2011) MYSO SED model fitter as we did in Paper I in order to investigate the physical properties of individual sources. Perhaps more well-known is the SED fitter by Robitaille et al. (2007), but their YSO models were developed mostly with the intention of fitting lower-mass protostars that are typically observed in lower pressure environments and with lower accretion rates than the massive protostars the ZT models were developed for. Some comparisons between the models fit to MYSO SEDs by both the ZT and Robitaille algorithms were given in De Buizer et al. (2017), and while some model parameters were shown to vary significantly between the two, the values for central stellar mass and bolometric luminosity (i.e., those parameters we are concerned with more here) were in fairly good agreement.

The ZT fitter pursues a χ^2-minimization to determine the best-fit MYSO models, with each model fit providing a normalized minimum χ^2 value (so-called $\chi^2_{\mathrm{nonlimit}}$). To be consistent with the analysis of Paper I, we selected a group of models that show $\chi^2_{\mathrm{nonlimit}}$ values similar to the best-fit model and distinguishable from the next group of models showing significantly larger $\chi^2_{\mathrm{nonlimit}}$ values. Typically, the jump in $\chi^2_{\mathrm{nonlimit}}$ value from one group to the next is a factor of 3 or more than the average separation of $\chi^2_{\mathrm{nonlimit}}$ values in the preceding group. Sometimes the first and/or second best fits have significantly lower $\chi^2_{\mathrm{nonlimit}}$ values than those that come in the grouping after, and in such cases, we will include those first fits with the first grouping so that we always have at least 5 best-fit models.

Figure 13 shows the ZT MYSO SED model fits as the solid lines (black for the best model fit, and gray for the rest in the group of best-fit models) on top of the derived photometry points for each individual source. Table 3 lists the physical properties of the MYSO SED model fits for each source. The observed bolometric luminosities, L_{obs}, of the best-fit models are presented in column 2, and the true total bolometric luminosities, L_{tot} (i.e., corrected for the foreground extinction and outflow viewing angles), are in column 3. The extinction and the stellar mass of the best models are listed in columns 4 and 5, respectively. In column 6, we provide the number of the models in the group of best model fits. Columns 7 and 8 present the ranges of the foreground extinction and stellar masses derived from the models in the group of best model fits in column 6. Column 9 shows the identification of the individual sources based on the previous studies as well as our criteria of MYSOs and possible MYSOs ("pMYSOs") set in Paper I. To summarize, the conditions for a source to be considered an MYSO are that it must (1) have an SED reasonably fit by the MYSO models, (2) have a $M_{\mathrm{star}} \geqslant 8\,M_{\odot}$ for the best model fit model, and (3) have a $M_{\mathrm{star}} \geqslant 8\,M_{\odot}$ for the range of M_{star} of the
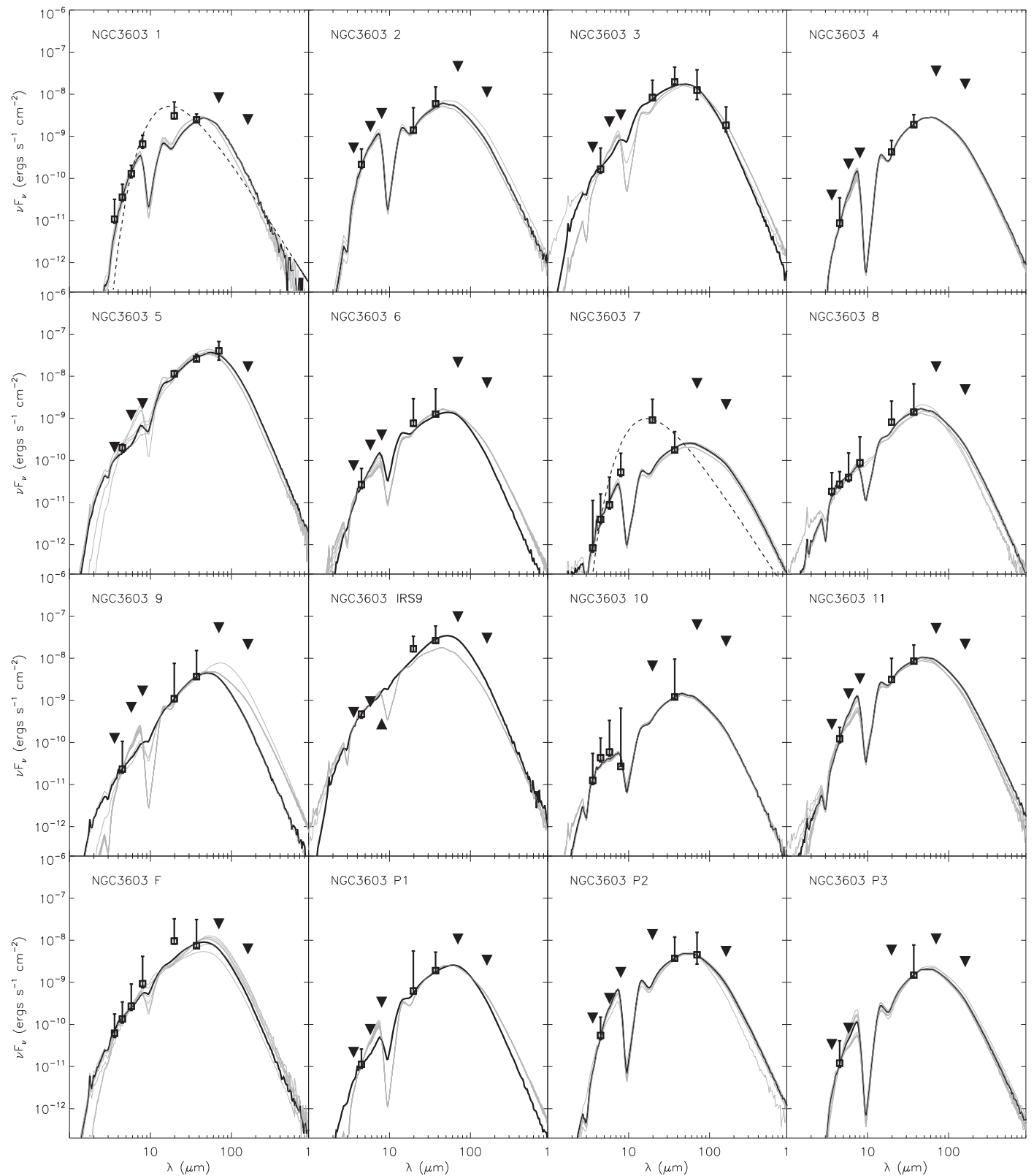
Figure 13. SED fitting with ZT model for compact sources in NGC 3603. Black lines are the best-fit model to the SEDs, and the system of gray lines is the remaining fits in the group of best fits (from Table 3). Upside-down triangles are data that are used as upper limits in the SED fits.

group of best-fit models. A pMYSO fulfills only the first two of these criteria.

We find that the multiwavelength photometry for 14 of the 16 compact sources with sufficient data sampling to create

SEDs can be well-fit by the MYSO models. Two sources, 1 and 7, appear to peak at 20 μm and are better fit with single temperature blackbodies (205 and 220 K, respectively; see Figure 13), and thus are thought to maybe be externally heated

Table 3
SED Fitting Parameters of Selected Compact Infrared Sources in NGC 3603

Source	L_{obs} $(\times 10^3 L_\odot)$	L_{tot} $(\times 10^3 L_\odot)$	A_v (mag)	M_{star} $(M_\odot)$	A_v Range (mag)	M_{star} Range $(M_\odot)$	Best Models	Notes
1	5.47	457.90	79.5	48.0	79.5–79.5	16.0–48.0	7	dust shell
2	14.15	78.27	62.9	24.0	57.0–74.6	16.0–32.0	6	MYSO
3	43.32	112.66	26.5	16.0	7.9–26.5	16.0–24.0	7	MYSO
4	6.51	9.45	31.9	8.0	28.5–39.4	8.0–8.0	13	MYSO
5	82.72	115.52	26.5	16.0	26.5–79.5	16.0–32.0	6	MYSO
6	3.41	13.30	53.0	8.0	8.4–53.0	8.0–8.0	10	MYSO
7	0.68	0.89	3.4	4.0	0.8–13.4	4.0–4.0	5	dust clump
8	3.90	10.18	5.9	8.0	5.9–10.9	8.0–16.0	10	MYSO
9	9.22	49.40	26.5	12.0	22.6–53.0	8.0–12.0	12	MYSO
10	3.21	28.78	34.4	16.0	9.2–36.9	8.0–16.0	8	MYSO
11	25.63	36.53	8.4	16.0	1.7–31.9	16.0–24.0	11	MYSO
IRS 9	76.15	976.81	26.5	64.0	1.7–26.5	32.0–64.0	6	MYSO
F	20.91	108.08	26.5	16.0	25.2–53.0	12.0–64.0	7	MYSO
P1	5.75	15.34	53.0	8.0	29.3–53.0	8.0–8.0	10	MYSO
P2	11.75	19.87	38.6	12.0	38.6–83.8	12.0–32.0	6	MYSO
P3	4.59	17.02	67.1	12.0	51.1–108.6	8.0–16.0	11	MYSO

Note. An "MYSO" in the right column denotes an MYSO candidate. Compact sources IRS 4 and source 12 are not tabulated due to lack of data points for the SED fitter.

dust shells or knots. Source F also has a slightly high 20 μm flux for the MYSO SED fitter, but it is less pronounced than those for sources 1 and 7. Slightly high 20 μm fluxes have been seen for one or two compact sources in almost every GH II region studied in this survey, and there is the potential that some spectral feature might be enhancing emission in this filter bandpass. In the second paper of this series (Lim et al. 2020; hereafter Paper II), we discuss that the [S III] at 18.71 μm could potentially be bright enough to affect the measured emission in this filter for some sources or regions. In any case, for source F, there are many nominal data points that are fit by the MYSO fitter, and we know that source F is a substantial radio continuum source and is indeed likely to be an MYSO (as the fits suggest). We note that no sources fulfill the pMYSO criteria in NGC 3603.

Of the 14 sources believed to be MYSOs based on the SED fitting, only 4 (F, P1, P2, and P3) have detected centimeter radio continuum emission. As mention previously, sources 4 and 5 do not lie within the confines of any of the high spatial resolution radio continuum data that we have access to, and thus, whether or not they have radio continuum emission is unknown. Five MYSOs (3, 9, 10, 11, and IRS 9) are located within extended diffuse radio continuum emission, but there are no radio continuum peaks at their locations, and thus, it is not clear if they are emitting radio continuum emission or not. For the eight MYSOs with no detectable radio emission (2, 6, and 8) or no peak above the extended continuum (3, 9, 10, 11, and IRS 9), it is possible that they are in a very young state prior to the onset of a hypercompact H II region (Hosokawa et al. 2010) and not observable via radio continuum emission.

Of all the MYSOs found in NGC 3603, the most massive is IRS 9 with a best-fit mass of 64 $M_\odot$. Both IRS 9 and source F top out at 64 $M_\odot$ in the range of best-fit model masses, meaning *no* source is fit with any model greater than this value. It is interesting that the most massive MYSO in the most powerful GH II region in the Galaxy (in terms of Lyman continuum flux) is smaller than the most massive MYSOs seen in the next two most powerful GH II regions we have studied, W49A (128 $M_\odot$) and W51A:G49.5-0.4 (96 $M_\odot$). Furthermore, compared to both

W49A (24) and W51A:G49.5-0.4 (37), NGC 3603 has a dearth of MYSOs in general (18). Put another way, W49A is 2 × fainter, and W51A:G49.5-0.4 is 4 × fainter in Lyman continuum flux than NGC 3603, but they contain 1.3 × and 2 × the number of MYSOs as NGC 3603, respectively. We will discuss a potential reason for this in Section 4.2.2.

4.2. Physical Properties of Extended Subregions: Evolutionary Analysis Methodology and Kinematic Status

The observations of CS by Nürnberger et al. (2002) and CO by Fukui et al. (2014) show that there appears to be a filament of molecular material present here extended ∼7′ to the north and ∼6′ to the south of the HD 97950 cluster. In the CS observations of Nürnberger et al. (2002), they identify 13 molecular clumps in this filament, which they label MM1 to MM13, and show that the HD 97950 cluster lies near the center of (and presumably formed from) the filament. The clumps MM1 and MM2 lie just to the south of the HD 97950 cluster and are the closest in projection. Slightly farther away and to the north of the stellar cluster are molecular clumps MM6 and MM7. Together, these four clumps are coincident with the brightest near- to mid-infrared emitting dust of NGC 3603 and, in particular, the brightest areas seen in our SOFIA maps (Figure 14). Using high spatial resolution 870 μm data from the APEX telescope,[7] and cross referencing it with ^{13}CO (1–0) archival data from the Mopra 22 m telescope of the Australia Telescope National Facility (project I.D.—M161; Barnes et al. 2018), we were able to confirm the locations and extents of these molecular clumps (i.e., the extended subregions) contained in our SOFIA fields, and these are shown in Figure 14. We tabulate the relevant information describing subregion locations, photometric apertures used, and measured SOFIA fluxes in Table 4 (with Spitzer and Herschel photometric data given in Appendix C).

---

[7] Based on observations under program ID 081.F-9325(A). APEX is a collaboration between the Max-Planck-Institut fuer Radioastronomie, the European Southern Observatory, and the Onsala Observatory.
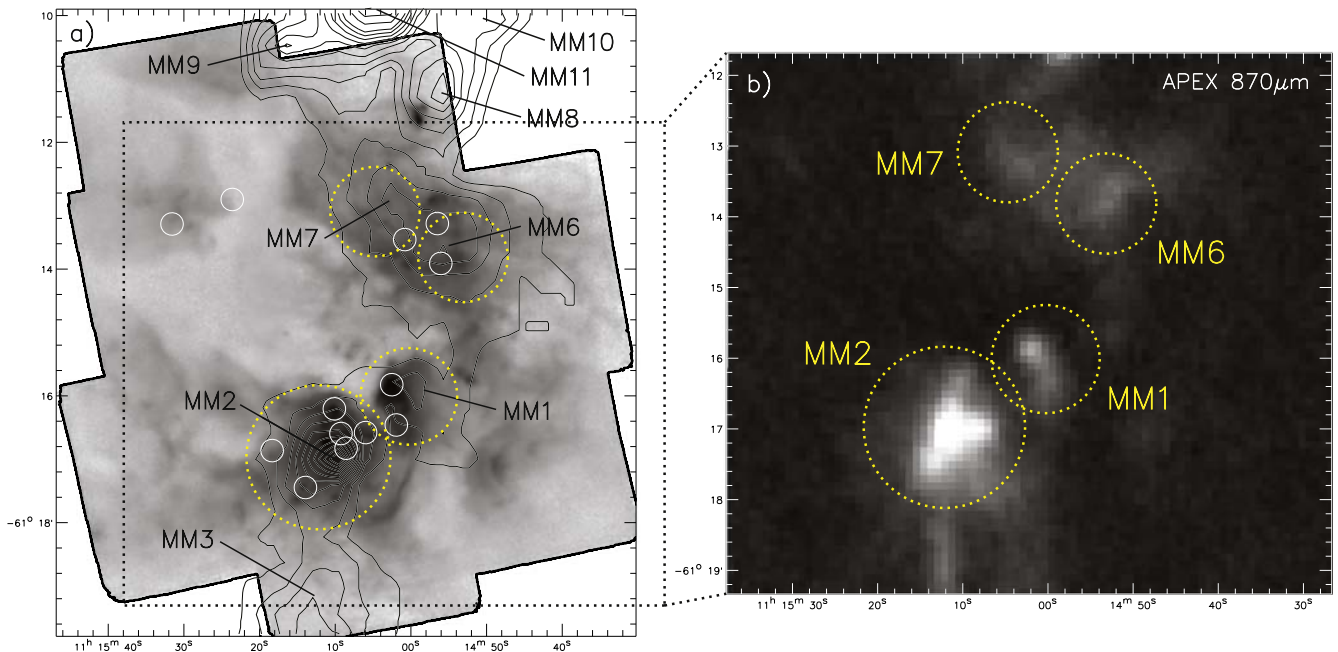
Figure 14. Extended subregions of NGC 3603 used for evolutionary analyses. (a) The background image is SOFIA 37 μm, and the black contours are the CS observations of Nürnberger et al. (2002) showing the major molecular clump locations (labeled MM1, MM2, etc.). White circles are the radio continuum peak locations from De Pree et al. (1999). Yellow dashed circles are the subregions defined in Table 4. (b) A slight zoom in on the dashed box in panel (a) showing the field at 870 μm as observed by APEX. Again, the size and locations of the subregions are marked.

Table 4
SOFIA Observational Parameters of Subregions within NGC 3603

Source	R.A. (J2000)	Decl. (J2000)	20 μm			37 μm		
			R_{int} (arcsec)	F_{int} (Jy)	F_{int-bg} (Jy)	R_{int} (arcsec)	F_{int} (Jy)	F_{int-bg} (Jy)
MM1	11:15:00.36	−61:16:00.6	46	4610	3640	46	6740	4640
MM2	11:15:12.18	−61:16:59.0	69	8350	7000	69	15,500	12,500
MM6	11:14:53.33	−61:13:49.3	43	1851	824	43	3610	1057
MM7	11:15:05.07	−61:13:06.6	42	2096	746	42	4340	1334

Note. Subregions are defined as large, contiguous regions, as seen in the CS, CO, and 870 μm maps.

As we did in our previous papers, we can use the SOFIA data along with gas kinematics information to study the evolutionary state of these extended subregions (assuming they are star-forming molecular clumps) and try to see if they give us clues as to how the region came together or evolved to its present state. In previous papers of this project, we conducted a comparative analysis between two independent tracers of molecular clump evolution: virial parameter and luminosity-to-mass ratio (L/M), focusing on individual extended sources within GH II regions. The analysis revealed a distinct positive correlation between the virial parameter (α_{vir}) and L/M for the subregions. Higher values of both α_{vir} and L/M were interpreted as indicative of relatively older subregions.

We extended this analysis to the extended subregions within NGC 3603. Overall, our approach was similar to that used in Paper I, but we we highlight here the key steps. First, to derive the L/M values, we determined the masses using a pixel-by-pixel graybody fitting method, following the technique developed by Lim et al. (2016). To achieve higher angular resolution, we utilized the Herschel 160 to 500 μm images and convolved them to a common beam size of 36″ to obtain a "template temperature" (T) map. Subsequently, we applied this temperature map to the APEX 870 μm data for improved

density mapping (i.e., $\sim$18″ resolution). Second, we calculated the bolometric luminosities (L) through a two-temperature graybody fit using the integrated total fluxes for each source in each Spitzer, SOFIA, and Herschel filter. Background flux estimation was performed using the data in an annulus outside of the photometric aperture of each extended source.

Then, to derive the virial parameters (α_{vir}) of each extended subregion, we followed the methods laid out in Paper I. In short, the virial analysis entails comparing the gravitational potential energy of extended sources to the total kinematic energy using the virial parameter ($\alpha_{vir} = M_{vir}/M$). In this study, the analysis involves calculating the latter from the full width at half maximum (FWHM) of the integrated ^{13}CO (1–0) line profiles of Mopra data for each of the clumps (see Equation (2) of Paper I).

Table 5 summarizes the physical parameters we derived for each star-forming clump, including the virial mass (M_{vir}), clump mass (M), bolometric luminosity (L), the derived warm and cold temperature components (T_{cold} and T_{warm}), the L/M, and the virial parameter (α_{vir}).

As shown in Table 5, the extended sources within NGC 3603 exhibit mass ranges from $212.9 M_\odot$ to $1560 M_\odot$, with an average mass ($\overline{M}$) of approximately $583 M_\odot$. In comparison, W51A

Table 5
Derived Parameters of Subregions in NGC 3603

Source	M_{vir} ($M_\odot$)	M ($M_\odot$)	L ($\times 10^4 L_\odot$)	T_{cold} (K)	T_{warm} (K)	L/M $L_\odot/M_\odot$	α_{vir}
MM1	1369	212.9	242	149.9	224.7	5680	6.43
MM2	3327	1560	625	142.5	230.5	2002	2.13
MM6	455.8	264.9	80.2	128.2	214.3	1514	1.72
MM7	1289	293.3	107	128.6	238.3	1821	4.39

(Paper I), M17 (Paper II), and W49A (De Buizer et al. 2021) have mean masses of approximately $3500 M_\odot$, $2100 M_\odot$, and $1400 M_\odot$, respectively. It is important to highlight that, despite being the most luminous GH II region in the Milky Way in terms of Lyman continuum luminosity (Conti & Crowther 2004; Paper IV), NGC 3603 exhibits much smaller $\overline{M}$ values for its molecular clumps compared to other GH II regions with similarly large N_{LyC} values (i.e., W49A and W51A).

This trend of lower mass and higher luminosity can be seen in our measured L/M values. The minimum and maximum L/M values for the extended sources in NGC 3603 are approximately $1500 L_\odot/M_\odot$ and $5700 L_\odot/M_\odot$, respectively. In contrast, W51A, W49A, and M17 show L/M ranges of $26 \lesssim L/M \lesssim 800 L_\odot/M_\odot$, $50 \lesssim L/M \lesssim 500 L_\odot/M_\odot$, and $300 \lesssim L/M \lesssim 2000 L_\odot/M_\odot$, respectively. Since larger L/M values denote more evolved sources (e.g., Krumholz & Tan 2007), this suggests that, globally, NGC 3603 is in a more advanced evolutionary stage compared to the other GH II regions studied in this project (although as we will discuss below, there may be an additional reason for the higher L/M values).

The derived dust temperatures based upon the graybody model employed also seem to indicate that NGC 3603 is an overall more evolved GH II region than the others. In Table 5, we list the T_{cold} and T_{warm} of the extended sources of NGC 3603, which span along the ranges of $128\,K \lesssim T_{cold} \lesssim 150\,K$ and $214\,K \lesssim T_{warm} \lesssim 238\,K$, respectively. Compared to the other GH II regions we have studied, the T_{cold} values for the NGC 3603 extended sources are 50–70 K higher, and higher temperatures are generally expected for more evolved clumps. This is also seen in Paper I, where the older population of molecular clumps in the G49.50.4 region (i.e., sources f–j) of W 51 A possess ∼20–30 K higher T_{cold} values compared to the younger clumps in the G49.50.3 and G49.50.4 regions.

Our virial analysis of the extended sources was used to assess the degree of kinematic stability within GH II regions and examine overall trends. The α_{vir} values for NGC 3603 ranged from 1.72 to 6.43. Among these, only one subregion (MM6) is gravitationally bound ($\alpha_{vir} < 2$), while the remaining three sources are unbound ($\alpha_{vir} > 2$). Unlike other GH II regions in this project, NGC 3603 did not exhibit any self-collapsing molecular clumps ($\alpha_{vir} < 1$). Therefore, the overall α_{vir} analysis aligns with the other analyses described above, indicating that NGC 3603 contains a relatively older clump population compared to other GH II regions.

To further investigate the evolutionary states of star-forming molecular clumps in NGC 3603, we created a plot of α_{vir} versus L/M, as depicted in Figure 15. We included clumps from previous studies in this project for comparison. Similar to W49A, the plot clearly illustrates that the range of relative ages of clumps in NGC 3603 is smaller than in W51A and M17. It is also discernible that the extended sources of NGC 3603 show higher L/M values than those of W51A and W49A relative to
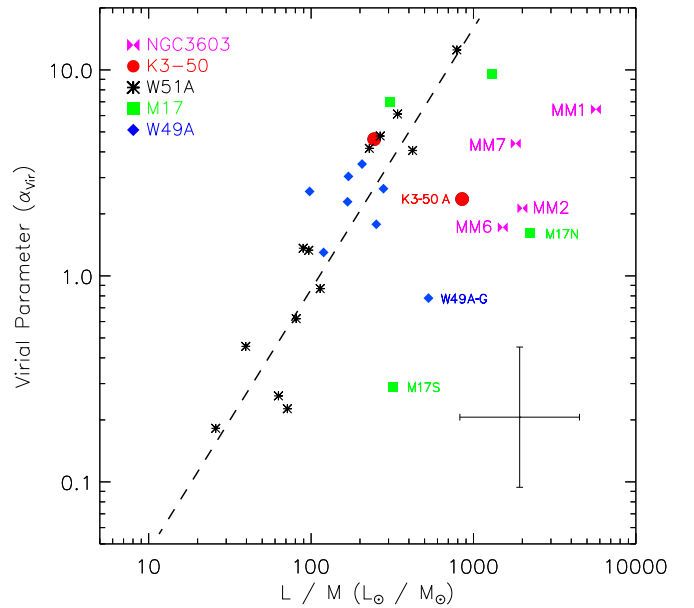

Figure 15. Virial parameter (α_{vir}) vs. L/M of all infrared subregions in all GH II regions studied so far. Black asterisks are values for the subregions in W51A (i.e., both the G49.5-0.4 and G49.4-0.3 GH II regions), and the dashed line indicates the best line fit to the W51A data ($\alpha \sim 1.28$ in log-space). Green squares show the subregions of M17, blue diamonds show the data for the subregions in W49A, and the red dots are for K3-50. All labeled subregions, including all subregions in NGC 3603, appear to have significantly higher L/M values that place them to the right of the main trend. These regions are believed to have higher L/M values due to contamination by external heating/ionization. The error bar at the bottom left shows the typical uncertainty (a factor of ∼2) in both L/M and α_{vir}.

their α_{vir} value so that NGC 3603 sources appear shifted to the right from the major trend of W51A and W49A in Figure 15. The L/M analysis is supposed to utilize measurements of the intrinsic luminosity and mass of the molecular clump; however, we argued in previous papers that the sources lying to the right of the main trend are likely to have heightened luminosity measurements (and therefore L/M values) due to external heating. For instance, for the two extended sources of M 17 (M17 N and M17 S), we suggested that external heating from the nearby evolved massive stellar cluster (NGC 6618) was affecting the SED of the surrounding molecular clumps (Paper II). Similarly, the extended sources in NGC 3603 are all likely to be heavily influenced by its central stellar cluster, HD 97590, which in turn augments the L/M values we derive. Therefore, in NGC 3603, the virial parameter may be a better indication of relative ages than the L/M values. With that being said, the location of all the data points in the upper right corner of Figure 15 is consistent with the clumps in NGC 3603 all being relatively older. Furthermore, the values for α_{vir} and L/M for clumps MM2, MM6, and MM7 are practically the same given the errors (see the error bars in Figure 15), indicating that the age spread of the clumps is also relatively small.

4.2.1. The Evolutionary History of NGC 3603

Our results from the compact source analyses show that there is a modest amount of massive star formation presently occurring, especially for a GH II region the size and power of NGC 3603 (more on this in Section 4.2.2). The star formation is also isolated to a small number of molecular cores (which are producing the MYSOs we see). However, none of the large

molecular clumps that make up NGC 3603 appear to be globally collapsing, and therefore may not produce a substantial subsequent star formation population in the future.

In terms of the evolutionary history of NGC 3603, Melnick et al. (1989) was the first to claim that there may be signs of sequential triggered star formation within the GH II region. They claimed that there is evidence of an older population of stars, pointing to the presence of several evolved stars in the area, like the BSGs Sher 18 and Sher 23 (Brandner et al. 1997b), as well as Sher 25, which Melnick et al. (1989) estimated to have formed ~10 Myr ago. Frogel et al. (1977) also claimed that IRS 4, IRS 5, IRS 6, and IRS 15 are late-type K and M supergiant stars, which Melnick et al. (1989) estimated to be on the order of 7 Myr old. Separate from this older collection of stars, the HD 97950 cluster itself has been determined by many groups to be much younger, at around ~1–3 Myr old (e.g., Eisenhauer et al. 1998; Brandl et al. 1999; Sung & Bessell 2004; Stolte et al. 2006; Melena et al. 2008). This led Melnick et al. (1989) to suggest that star formation occurred in two epochs (one ~10 Myr ago and the other ~1 Myr ago). Furthermore, Melnick et al. (1989) suggest that the older stars appear to be concentrated to the north, and so, perhaps, the star formation may have proceeded from the north (i.e., around the MM1 and MM2 subregions) to south of the HD 97950 cluster (i.e., around the MM2 subregion), and this might indicate some form of sequential star formation.

Our evolutionary analyses show that clump MM6 to the west is the youngest, and clump MM1 in the southwest is oldest, with MM7 to the north and MM2 to the south being at some relative age in between. There is therefore no obvious age trend north–south, which seems to contradict the sequential north–south star formation scenario of Melnick et al. (1989). Nor does there seem to be a trend east–west or inside out either, signifying that there may be no globally triggered sequential star formation of any kind occurring in NGC 3603. Indeed, as we have seen from the GAIA distances to the IRS sources (Table 1), they are not physically associated with NGC 3603. Furthermore, looking at the the GAIA distances for the BSGs Sher 25 (5873^{+30}_{-102} pc) and Sher 18 (4274^{+54}_{-94} pc) shows that they too are not part of NGC 3603. Thus, the fact that the majority of these evolved sources lie (in projection) more to the north of HD 97950 (as pointed out by Melnick et al. 1989) and seem to have formed at a different epoch compared to the cluster is irrelevant to the evolutionary history of NGC 3603.

The second hypothesis for the evolution of NGC 3603 comes from Fukui et al. (2014), who suggest that the present state of NGC 3603 was the result of a cloud–cloud collision. They find evidence in their CO data for molecular material at two discrete velocities, one at 13 km s^{-1} and the other at 28 km s^{-1}. The molecular material detected at these velocities covers almost the entire filament as seen in the Nürnberger et al. (2002) CS maps (i.e., the region covering MM1-MM13). Fukui et al. (2014) claim that the two clouds collided with each other ~1 Myr ago instigating a burst of star formation that led to the creation of most of the stars in the area, including the HD 97950 star cluster.

The fact that we find a relative small age spread in the clump ages of NGC 3603 would seem to support the idea that the majority of star formation may have occurred around the same time, which may be consistent with the cloud–cloud collision scenario. The mid-infrared MYSOs we identified in this work, the YSOs found in the studies by others (e.g., Frogel et al. 1977;

Nürnberger & Stanke 2003; Di Cecco et al. 2015), the massive proplyd candidates (Brandner et al. 2000; Mücke et al. 2002), as well as the presence of maser emission from water, methanol, and OH species (e.g., Caswell et al. 1989; Caswell 2004; Breen et al. 2010), all provide evidence or recent star formation activity, however, at a very modest level, as mentioned above. Furthermore, Fukui et al. (2014) suggest that the moderate collection of older stars seen in the area is also evidence that there was only modest star formation activity before the cloud–cloud collision as well (and we additionally now know most of them are foreground stars).

4.2.2. Two Types of GH II Regions?

In Paper IV, we proposed the utilization of various secondary criteria to potentially distinguish whether a given region qualifies as a genuine GH II region or not, especially in cases where the N_{LyC} value as measured from the centimeter radio continuum flux exhibits a considerable error or is in close proximity to the qualifying threshold. The suggested supplementary indicators were as follows: the number of compact infrared sources within the region, the number of subregions it comprises, the proportion of the total infrared flux emanating from the brightest source within the region, and the mass of the most massive MYSO. In Paper V, we discuss that there was evidence suggesting that the population of GH II regions may exhibit two distinct morphological variations, one characterized by dispersed radio subregions (i.e., "distributed-type") and the other marked by contiguous cavity structures (i.e., "cavity-type"). The evolutionary pathways, and consequently the observed properties, of a GH II region may vary significantly between the two morphological classifications, hinting at the possibility that the aforementioned indicators could be an oversimplification.

Indeed, NGC 3603 has a cavity-like morphology similar in appearance to the previously studied M17 and DR7 GH II regions in our survey. We add the values for the supplementary indicators discussed above to those for the other sources we have observed in this survey with log$N_{LyC} > 50.0$ and list them in Table 6. These regions are listed in order by N_{LyC} value, and a horizontal line separates those with similar values, i.e., those with $51.02 < N_{LyC} < 51.61$ and those with $50.07 < N_{LyC} < 50.22$. For the four sources with a higher range of N_{LyC}, it can be seen that the two with a cavity-type morphology have similar but lower values in all indicators, when compared to those with a distributed-type morphology, which have higher values in all indicators. Likewise, for the three regions with a lower range of N_{LyC}, the cavity-type GH II region is an outlier with lower indicators as well. We do caution that these are small number statistics, and we will continue to investigate this issue as we continue our survey in future papers.

Nevertheless, as first discussed in Paper V, these two morphological classes of GH II region might point to a fundamentally different formation history. NGC 3603, along with M17 and DR7, are predominantly characterized by cavity structures, where a previously formed stellar cluster appears to be responsible for the vast majority of the ionization and dust heating within the cavity. In contrast, the other regions (W51A: G49.5-0.4, W51A:G49.4-0.3, W49A, and K3-50) consist of dusty, ionized subregions within larger molecular clumps with recent and ongoing massive star formation, contributing significantly to the overall Lyman continuum flux. In these regions, previous star formation likely plays a smaller role.

Table 6
Infrared Observational Indicators of All Surveyed GH II Regions to Date

Region	$\log N_{Lyc}$ (log s^{-1})	GH II Type	No. Compact Sources	No. Subregions	Flux in Peak (%)	Highest-mass YSO ($M_\odot$)
NGC 3603	51.61	Cavity	18	4	3	64
W49A	51.42	Distributed	24	15	25	128
W51A: G49.5-0.4	51.03	Distributed	37	10	20	96
M17	51.02	Cavity	16	4	5	64
W51A: G49.4-0.3	50.22	Distributed	10	5	15	64
DR7	50.10	Cavity	4	1	15	16
K3-50	50.07	Distributed	10	5	59	48

Cavity-type sources may have experienced intense star formation in the past, resulting in radiation pressure that initially prevented the formation of subsequent stars. Over time, this pressure cleared surrounding material until over-densities in the cavity walls became dense enough to locally collapse into new stars. For NGC 3603, M17, and DR7, it can be seen that MYSOs and compact sources are concentrated near these cavity walls. These regions may have fewer MYSOs overall, possibly indicating that they are more evolved GH II regions or are in a transitional state between major star formation events. Moreover, cavity-type regions like NGC 3603 exhibit a lack of extended subregions, with most of the infrared and radio emission originating from the ridges outlining the cavity walls being carved out of the larger molecular cloud. As a result, the suggested observation indicators for GH II regions that were suggested originally in Paper IV may not be reliable indicators of GH II region status for regions with a cavity-type morphology. As a consequence, the assessment of Paper IV that DR7 may not be a genuine GH II region may not be correct, and an evaluation of more sources will be required to better understand the observational properties of both GH II morphological classes.

5. Summary

We obtained SOFIA-FORCAST 20 and 37 μm maps toward NGC 3603, covering the brightest central infrared-emitting area ($\sim 8.'5 \times 8.'5$) of the GH II region at $\lesssim 3''$ spatial resolution. These infrared observations represent the best spatial resolution images yet of NGC 3603 at wavelengths more than 25 μm. In order to examine the morphological and physical characteristics of the compact sources and extended subregions within NGC 3603, we compared these SOFIA-FORCAST images with earlier multiwavelength studies spanning the near-infrared to radio wavelengths from various ground- and space-based telescopes. We used an MYSO SED model fitting algorithm to deduce properties of the compact infrared sources, and applied evolutionary analyses to the extended subregions within NGC 3603 under the assumption that they trace star-forming molecular clumps. We itemize below our main conclusions from this work.

(1) The SOFIA 20 and 37 μm images show similar large-scale structures. However, there is a distinct heating pattern that can be seen between the two wavelengths, with the 20 μm emission more strongly tracing hotter dust nearer to the HD 97590 stellar cluster. At these wavelengths, emission can also be seen coming from the various known pillars and trunks, all of which point back to the central stellar cluster.

(2) There are three proplyd-candidates previously identified in NGC 3603; however, it was unclear if they possessed circumstellar disks like the archetypical Orion proplyds. They are also more than an order of magnitude larger and have radio continuum emission; though, it was unclear if that emission is due to external or internal ionization. With SOFIA, all three sources are detected in the infrared, suggesting that they do indeed possess circumstellar dust of some kind, likely from both a disk and an envelope. While the Orion proplyds contain low-mass stars, our SED modeling shows that these sources are indeed likely to be massive, and thus, it is unclear if they are high-mass proplyds analogs or cometary-shaped UCH II regions.

(3) Sher 25 is an evolved BSG in the foreground of NGC 3603 that is surrounded by a circumstellar ring with bipolar outflow clouds that are believed to be part of a larger hourglass-shaped circumstellar nebula. Our SOFIA 20 μm image shows dust emission present around the entire circumstellar ring with infrared dust clumps well-correlated with the clumps seen in the Hubble Hα image. The outflow clouds are more prominent at 37 μm, and we argue that their dust is cooler than the dust in the circumstellar ring. We also detect faint emission from the entire hourglass nebula structure at 20 μm, confirming its presence.

(4) Frogel et al. (1977) identified and labeled infrared sources in the field of NGC 3603, with IRS 1–IRS 3 being identified in their 10 and 20 μm images, and IRS 4–IRS 15 being identified in their 2 μm images. Our SOFIA 20 and 37 μm images show no source at the location of IRS 3, and no source can be seen in the Spitzer or Herschel data either. IRS 4–IRS 15 are quoted with $10''$ astrometric accuracy by Frogel et al. (1977), and we use 2MASS data to identify these sources and refine their coordinates. IRS 4 and IRS 9 are the only near-infrared-defined sources detected in our SOFIA mid-infrared data. IRS 4 is the brightest stellar object in all of NGC 3603 in the near-infrared but decreases in flux quickly with increased wavelength. Its distance, as deduced from GAIA parallax measurements, is only 3.4 kpc away, and it is therefore a foreground stellar source and not a YSO. Similarly, we find that most of the remaining IRS sources with no SOFIA detections but for which GAIA distances are available are also foreground stars unrelated physically to NGC 3603.

(5) We found 18 compact sources in the SOFIA data, and 8 are newly identified here. Sixteen sources had sufficient photometry data from SOFIA, Spitzer-IRAC,

and Herschel-PACS to construct SEDs. We fit those SEDs with YSO models and found 14 of the 16 sources (88%) are likely to be MYSOs, several of which are identified as such in this work for the first time. Sources 1 and 7, however, appear to be better fit with single temperature blackbodies, and we suggest that they may be externally heated dust shells or knots. Fourteen of the total 18 compact sources do not have radio continuum components, implying very young states of formation. However, two of the remaining four sources are located outside our radio continuum maps, so whether they have associated radio continuum emission is unknown.

(6) We calculated the L/M and virial parameters ($\alpha_{\rm vir}$) of the extended subregions of NGC 3603 to estimate their relative ages. Unlike other GH II regions in this project, NGC 3603 does not seem to have any self-collapsing molecular clumps ($\alpha_{\rm vir} < 1$), indicating that it is an older GH II region overall. Consistent with this, NGC 3603 was also found to have a much higher range of L/M ratios compared to the other GH II regions (although external heating complicates the interpretation). Further evidence of this comes from our derivations of dust temperature, which show that the star-forming clumps in NGC 3603 have much higher cold dust temperatures, which are generally expected for more evolved molecular clumps.

(7) The absence of discernible age trends in various directions of the molecular clumps within NGC 3603 suggests that there is no globally triggered sequential star formation occurring, but instead, the relatively small age spread among clumps supports the idea of synchronized star formation, perhaps consistent with the cloud–cloud collision formation scenario.

(8) Although it is the most powerful GH II region in the Galaxy based upon its Lyman continuum photon rate, the most massive MYSO in NGC 3603 is estimated to be only 64 $M_\odot$, which is significantly smaller than the most massive MYSOs seen in the next two most powerful GH II regions we have studied, W49A and W51A:G49.5-0.4. It also has far fewer MYSOs and extended infrared subregions. We argue that there are two classes of GH II region, and that NGC 3603 belongs to the *cavity-type*, which tend to have fewer YSOs, subregions, and more modest MYSO masses, whereas W49A and W51A: G49.5-0.4 belong to a *distributed-type* with very different observational properties in the infrared.

Appendix A
Data Release

The FITS images used in this study are publicly available at the following: https://dataverse.harvard.edu/dataverse/SOFIA-GHII. The data include the SOFIA FORCAST 20 and 37 μm final image mosaics of NGC 3603 and their exposure maps.

Appendix B
Distance to NGC 3603

The distance to NGC 3603 of 7.2 ± 0.1 kpc from Drew et al. (2019) was based upon parallax measurements from the GAIA mission's DR2. A more recent calculation based upon GAIA Early Data Release 3 (EDR3) data by Maíz Apellániz et al. (2022) yields a distance of 7130^{+590}_{-500} pc. Since these two distance measurements are equal to within their errors, we adopt here the value from Drew et al. (2019) because it is quoted with smaller uncertainty. However, an even more recent result based upon GAIA EDR3 data published just prior this article by Weßmayer et al. (2023) yields a closer distance with equally small uncertainty of 6250 ± 150 pc. To derive this value, Weßmayer et al. (2023) only used stars from an $r \sim 1'$ area centered on HD 97950, and rejected many stars previously included in the distance analyses of others on the basis of potentially discrepant proper motions and/or the fact that the stars did not match the 1–2 Myr isochrone of Melena et al. (2008). In the end, only 10 stars were used to determine the distance to NGC 3603 (compared to 288 stars used by Drew et al. 2019; and 166 by Maíz Apellániz et al. 2022). Interestingly, Drew et al. (2019) also derive a distance using the GAIA DR2 data for just the inner $1'$ of NGC 3603 and derive a much larger value of 8.2 ± 0.4 kpc using the parallaxes of just 30 stars. Moreover, Melena et al. (2008) summarize many of the distance measurements to NGC 3603, and a value of 6250 pc would be placed among the nearest distances reported, but consistent to within the errors of most measurements, which average closer to 7 kpc.

We reran the SED fitting algorithm for all compact sources under the assumption that the distance was at 6250 pc (instead of 7200 pc) and found that our results did not change significantly. The infrared sources identified in Table 3 as MYSOs are all still MYSOs at this slightly closer distance. The main differences are that, at the closer distance, IRS 9 has a best-fit model of only 32 $M_\odot$ (rather than 64 $M_\odot$), and the range of fits for all sources tops out at 32 $M_\odot$ (again, rather than 64 $M_\odot$). In general, the range of A_V of the best-fit SED models is lower at the closer distance, and either the lower limit or upper limit value in the mass range decreases by one mass step (the SED models have discrete masses of 2, 4, 8, 12, 16, 24, 32, 48, 64, 128 $M_\odot$). However, at this closer distance, still no source has a lower limit mass below 8 $M_\odot$. The mass derived from the best model fit for half of the sources (i.e., 8/16) changes (either higher or lower) by one mass step, while the other half are unaffected.

The results of the extended source analyses are also mildly affected, with calculations at the nearer distance yielding $\alpha_{\rm vir}$ and L/M values still within our quoted uncertainty level (a factor of 2) for all extended sources. Specifically, at a

distance of 6250 pc, the $\alpha_{\rm vir}$ values of each extended source increase by $\sim$16% while L/M remains the same (both L and M decrease by $\sim$26% on each source). The virial parameters show the range of $2.00 \lesssim \alpha_{\rm vir} \lesssim 7.46$ at 6250 pc while the range is $1.72 \lesssim \alpha_{\rm vir} \lesssim 6.43$ at our adopted distance. The overall trend seen in Figure 15 stays the same for $\alpha_{\rm vir}$ versus L/M at the 6250 pc distance, leaving the conclusions from the discussion in Section 4.2.1 unaffected.

Appendix C
Additional Photometry of Compact and Extended Sources in NGC 3603

In addition to the fluxes derived from the SOFIA-FORCAST data, we used derived photometry data in our SED analyses for our sources from both Spitzer-IRAC and Herschel-PACS.

As we mentioned in Section 4.1, we performed optimal extraction photometry on the FORCAST 20 and 37 μm images to define the location of all compact sources, and to determine the aperture radii to be used for photometry. As was done in our previous papers, using these derived source locations, we employed the same optimal extraction technique on the Spitzer-IRAC data and Herschel-PACS data for all compact sources to find the optimal aperture for each wavelength and derive their fluxes. However, performing the optimal extraction technique on the Herschel-PACS data failed for all sources but Source 3 due to contamination from extended emission from other nearby sources and/or bright environmental emission. For the contaminated compact sources in the Herschel-PACS data, we used an aperture that best fit the largest size of the source at any wavelength to derive flux estimates within the aperture, but do not derive background-subtracted photometry values. We additionally performed photometry on the extended subregions using the Spitzer-IRAC, Herschel-PACS, and Herschel-SPIRE data. Using the optimal extraction technique for each subregion, we derived background-subtracted fluxes for MM1, MM2, MM6, and MM7. Table 7 shows the photometry values we derived for all compact sources from the Spitzer-IRAC data, and Table 8 shows the values for the extended subregions. Table 9 shows the photometry values for all compact sources as derived from the Herschel-PACS data.

Table 7
Spitzer-IRAC Observational Parameters of Compact Sources in NGC 3603

Source	3.6 μm			4.5 μm			5.8 μm			8.0 μm		
	$R_{\rm int}$ (arcsec)	$F_{\rm int}$ (mJy)	$F_{\rm int-bg}$ (mJy)	$R_{\rm int}$ (arcsec)	$F_{\rm int}$ (mJy)	$F_{\rm int-bg}$ (mJy)	$R_{\rm int}$ (arcsec)	$F_{\rm int}$ (mJy)	$F_{\rm int-bg}$ (mJy)	$R_{\rm int}$ (arcsec)	$F_{\rm int}$ (mJy)	$F_{\rm int-bg}$ (mJy)
1	6.0	38.4	13.0	7.2	109	54.1	7.2	394	250	8.4	2820	1740
2	16	630	373	16	750	324	16	3290	1860	16	9280	4990
3	12	661	237	12	792	249	12	4250	1820	12	8570	2900
4	4.2	47.9	7.75	4.2	51.0	12.8	4.2	423	104	4.2	1070	341
5	4.8	245	185	4.8	365	300	7.2	2280	1480	7.2	5920	4090
6	5.4	88.8	45.7	5.4	96.7	40.1	5.4	446	235	5.4	1070	499
7	3.0	9.46	0.703	3.6	22.8	5.72	3.6	76.7	16.9	4.2	396	139
8	4.2	61.4	21.9	4.2	80.5	40.5	4.2	290	76.0	4.2	969	234
9	5.4	149	33.0	5.4	160	35.3	6.0	1310	227	6.0	4420	748
10	3.6	67.7	15.5	4.8	189	64.6	4.8	642	114	4.2	1730	71.7
11	7.2	321	181	7.2	343	184	9.0	2750	1350	9.0	8660	3610
12	⋯	sat	sat	⋯	sat	sat	⋯	sat	sat	⋯	sat	sat
IRS 4	⋯	sat	sat	⋯	sat	sat	⋯	sat	sat	⋯	sat	sat
IRS 9	3.0	615	540	3.0	814	706	3.0	1780	1250	⋯	sat	sat
F	7.8	212	74.1	7.8	515	202	7.8	1760	522	7.8	11,000	2470
P1	3.6	26.0	13.0	3.6	38.0	16.6	4.2	146	42.4	4.8	900	222
P1	3.6	26	13	3.6	38	16.6	4.2	146	42.4	4.8	900	222
P2	9.0	170	73.3	9.0	223	81.9	9.0	803	275	9.0	4570	2170
P3	4.8	40.5	12.7	4.8	60	17.6	4.8	157	35.3	⋯	sat	sat

Note. Entries with "sat" mean the sources are themselves saturated in that band or are affected by array saturation effects from nearby bright sources. If they are saturated themselves, we use the point-source saturation fluxes of 190, 200, 1400, and 740 mJy at 3.6, 4.5, 5.8, and 8.0 μm, respectively (from the Spitzer Observers Manual, Version 7.1.), as lower limits in the SED modeling.

Table 8
Spitzer-IRAC Observational Parameters of Subregions in NGC 3603

Source	3.6 μm			4.5 μm			5.8 μm			8.0 μm		
	$R_{\rm int}$ (arcsec)	$F_{\rm int}$ (Jy)	$F_{\rm int-bg}$ (Jy)	$R_{\rm int}$ (arcsec)	$F_{\rm int}$ (Jy)	$F_{\rm int-bg}$ (Jy)	$R_{\rm int}$ (arcsec)	$F_{\rm int}$ (Jy)	$F_{\rm int-bg}$ (Jy)	$R_{\rm int}$ (arcsec)	$F_{\rm int}$ (Jy)	$F_{\rm int-bg}$ (Jy)
MM1	46.2	5.78	3.27	46.2	10.4	7.32	46.2	39.2	28.2	⋯	sat	sat
MM2	69.0	17.6	12.5	69.0	25.4	18.9	69.0	115	90.7	⋯	sat	sat
MM6	43.0	3.61	1.33	43.0	5.07	1.17	43.0	18.9	2.88	⋯	sat	sat
MM7	42.2	6.73	4.14	42.2	7.73	4.70	42.2	31.3	9.95	⋯	sat	sat

Note. Entries with "sat" mean the subregions are affected by array saturation effects from bright sources.

Table 9
Herschel-PACS Observational Parameters of Compact Sources in NGC 3603

Source	70 μm			160 μm		
	R_{int} (arcsec)	F_{int} (Jy)	F_{int-bg} (Jy)	R_{int} (arcsec)	F_{int} (Jy)	F_{int-bg} (Jy)
1	16.0	191	⋯	22.5	133	⋯
2	16.0	1070	⋯	22.5	598	⋯
3	16.0	889	291	22.5	267	97.1
4	16.0	830	⋯	22.5	926	⋯
5	22.5	1560	939	22.5	894	⋯
6	16.0	496	⋯	22.5	373	⋯
7	16.0	157	⋯	22.5	114	⋯
8	16.0	392	⋯	22.5	254	⋯
9	16.0	1230	⋯	22.5	1120	⋯
10	16.0	1450	⋯	22.5	1340	⋯
11	16.0	1190	⋯	22.5	1140	⋯
12	16.0	83.2	⋯	22.5	69.0	⋯
IRS 4	16.0	389	⋯	22.5	241	⋯
IRS 9	16.0	2240	⋯	22.5	1590	⋯
F	16.0	569	⋯	22.5	331	⋯
P1	16.0	249	⋯	22.5	178	⋯
P2	16.0	358	105	22.5	288	⋯
P3	16.0	250	⋯	22.5	165	⋯

Note. If there is no F_{int-bg} value for a source, then the source is not well resolved from other nearby sources and/or extended emission. For these sources, the F_{int} value is used as the upper limit in the SED modeling.

Table 10
Herschel-PACS Observational Parameters of Subregions in NGC 3603

Source	70 μm			160 μm		
	R_{int} (arcsec)	F_{int} (Jy)	F_{int-bg} (Jy)	R_{int} (arcsec)	F_{int} (Jy)	F_{int-bg} (Jy)
MM1	44.8	5010	2840	44.8	1980	891
MM2	70.4	17,600	13,600	70.4	7850	4710
MM6	43.0	3900	1600	43.0	1470	639
MM7	42.4	4950	2790	42.2	1660	848

Table 11
Herschel-SPIRE Observational Parameters of Subregions in NGC 3603

Source	250 μm			350 μm			500 μm		
	R_{int} (arcsec)	F_{int} (Jy)	F_{int-bg} (Jy)	R_{int} (arcsec)	F_{int} (Jy)	F_{int-bg} (Jy)	R_{int} (arcsec)	F_{int} (Jy)	F_{int-bg} (Jy)
MM1	46.2	551	216	44.8	182	49.6	42.2	72.6	27.7
MM2	69.0	2670	2120	70.4	958	738	42.2	343	216
MM6	43.0	504	232	43.0	188	81.8	42.2	80.9	14.8
MM7	42.4	583	161	42.2	208	106	42.2	77.2	37.2

Tables 10 and 11 show the photometry values for all extended subregions, as derived from the Herschel-PACS data and Herschel-SPIRE data, respectively.

ORCID iDs

James M. De Buizer https://orcid.org/0000-0001-7378-4430
Wanggi Lim https://orcid.org/0000-0003-4243-6809
Nicole Karnath https://orcid.org/0000-0003-3682-854X
James T. Radomski https://orcid.org/0000-0003-0740-2259

References

Bally, J., O'Dell, C. R., & McCaughrean, M. J. 2000, AJ, 119, 2919
Barnes, P. J., Hernandez, A. K., Muller, E., et al. 2018, ApJ, 866, 19
Brandl, B., Brandner, W., Eisenhauer, F., et al. 1999, A&A, 352, L69
Brandner, W., Chu, Y.-H., Eisenhauer, F., et al. 1997a, ApJL, 489, L153
Brandner, W., Grebel, E. K., Chu, Y.-H., et al. 1997b, ApJL, 475, L45
Brandner, W., Grebel, E. K., Chu, Y.-H., et al. 2000, AJ, 119, 292
Breen, S. L., Caswell, J. L., Ellingsen, S. P., et al. 2010, MNRAS, 406, 1487
Burrows, C. J., Krist, J., Hester, J. J., et al. 1995, ApJ, 452, 680
Caswell, J. L. 2004, MNRAS, 351, 279
Caswell, J. L., Batchelor, R. A., Forster, J. R., et al. 1989, AuJPh, 42, 331
Conti, P. S., & Crowther, P. A. 2004, MNRAS, 355, 899

Cutri, R. M., Skrutskie, M. F., van Dyk, S., et al. 2003, yCat, II/246
De Buizer, J. M., Lim, W., Karnath, N., et al. 2022, ApJ, 933, 60
De Buizer, J. M., Lim, W., Liu, M., et al. 2021, ApJ, 923, 198
De Buizer, J. M., Lim, W., Radomski, J. T., et al. 2023, ApJ, 949, 82
De Buizer, J. M., Liu, M., Tan, J. C., et al. 2017, ApJ, 843, 33
De Pree, C. G., Nysewander, M. C., & Goss, W. M. 1999, AJ, 117, 2902
Di Cecco, A., Faustini, F., Paresce, F., et al. 2015, ApJ, 799, 100
Drew, J. E., Monguió, M., & Wright, N. J. 2019, MNRAS, 486, 1034
Eisenhauer, F., Quirrenbach, A., Zinnecker, H., et al. 1998, ApJ, 498, 278
Frogel, J. A., Persson, S. E., & Aaronson, M. 1977, ApJ, 213, 723
Fukui, Y., Ohama, A., Hanaoka, N., et al. 2014, ApJ, 780, 36
Gaia Collaboration 2020, yCat, I/350
Goss, W. M., & Radhakrishnan, V. 1969, ApL, 4, 199
Gutermuth, R. A., Megeath, S. T., Myers, P. C., et al. 2009, ApJS, 184, 18
Gvaramadze, V. V., Kniazev, A. Y., Chene, A.-N., et al. 2013, MNRAS, 430, L20
Hendry, M. A., Smartt, S. J., Skillman, E. D., et al. 2008, MNRAS, 388, 1127
Herter, T. L., Vacca, W. D., Adams, J. D., et al. 2013, PASP, 125, 1393
Hofmann, K.-H., Seggewiss, W., & Weigelt, G. 1995, A&A, 300, 403
Hosokawa, T., Yorke, H. W., & Omukai, K. 2010, ApJ, 721, 478
Krumholz, M. R., & Tan, J. C. 2007, ApJ, 654, 304
Lacy, J. H., Beck, S. C., & Geballe, T. R. 1982, ApJ, 255, 510
Lim, W., & De Buizer, J. M. 2019, ApJ, 873, 51
Lim, W., De Buizer, J. M., & Radomski, J. T. 2020, ApJ, 888, 98

Lim, W., Tan, J. C., Kainulainen, J., et al. 2016, ApJL, 829, L19
Maíz Apellániz, J., Barbá, R. H., Fernández Aranda, R., et al. 2022, A&A, 657, A131
Melena, N. W., Massey, P., Morrell, N. I., et al. 2008, AJ, 135, 878
Melnick, J., Tapia, M., & Terlevich, R. 1989, A&A, 213, 89
Moffat, A. F. J. 1983, A&A, 124, 273
Moffat, A. F. J., Drissen, L., & Shara, M. M. 1994, ApJ, 436, 183
Mücke, A., Koribalski, B. S., Moffat, A. F. J., et al. 2002, ApJ, 571, 366
Nürnberger, D. E. A. 2003, A&A, 404, 255
Nürnberger, D. E. A., Bronfman, L., Yorke, H. W., et al. 2002, A&A, 394, 253
Nürnberger, D. E. A., & Stanke, T. 2003, A&A, 400, 223
O'Dell, C. R., Wen, Z., & Hu, X. 1993, ApJ, 410, 696
Retallack, D. S., & Goss, W. M. 1980, MNRAS, 193, 261
Robitaille, T. P., Whitney, B. A., Indebetouw, R., et al. 2007, ApJS, 169, 328
Rochau, B., Brandner, W., Stolte, A., et al. 2010, ApJL, 716, L90
Röllig, M., Kramer, C., Rajbahak, C., et al. 2011, A&A, 525, A8
Sher, D. 1965, MNRAS, 129, 237
Stolte, A., Brandner, W., Brandl, B., et al. 2006, AJ, 132, 253
Sung, H., & Bessell, M. S. 2004, AJ, 127, 1014
Wang, J., & Chen, Y. 2010, SCPMA, 53, 271
Weßmayer, D., Przybilla, N., Ebenbichler, A., et al. 2023, A&A, 677, A175
Young, E. T., Becklin, E. E., Marcum, P. M., et al. 2012, ApJL, 749, L17
Zhang, Y., & Tan, J. C. 2011, ApJ, 733, 55
Zinnecker, H., & Yorke, H. W. 2007, ARA&A, 45, 481